universität wien

MASTERARBEIT | MASTER'S THESIS

Titel | Title

Investigating Structural Changes in the Gβγ Pathological Variant I80T Associated with GNB1 Encephalopathy

verfasst von | submitted by

Alexandra Čapkovičová Bc.

angestrebter akademischer Grad | in partial fulfilment of the requirements for the degree of

Master of Science (MSc)

Wien | Vienna, 2024

Studienkennzahl lt. Studienblatt | Degree programme code as it appears on the student record sheet:	UA 066 606
Studienrichtung lt. Studienblatt | Degree programme as it appears on the student record sheet:	Masterstudium Drug Discovery and Development
Betreut von | Supervisor:	Assoz. Prof. Mag. Dr. Anna Weinzinger Privatdoz.

Acknowledgements

First and foremost, I would like to express my gratitude to Assoc. Prof. Priv. Doz. Dr. Anna Weinzinger for giving me the opportunity to join her research group and supervising my work. Secondly, I would like to express my gratitude to Theres Friesacher, BSc MSc for her invaluable support, mentorship and great willingness to always help me overcome obstacles all throughout the research process. I am very grateful to Mag. pharm. Michael Jirout, PhD for his guidance during my beginnings and for his patience when introducing me into the complex principles of molecular dynamics simulations.

Moreover, I would like to thank my family and close friends who have continuously supported me throughout my studies and for being patient and understanding during this demanding period. I express the greatest appreciation to everyone who has helped me during my academic journey.

Abstract

G protein coupled inwardly rectifying potassium (GIRK) channels play a vital role in inhibitory neurotransmission by hyperpolarizing neurons and silencing cellular electrical activity. Mutations often lead to diminished activity of GIRK channels and result in a variety of neurological disorders. Missense variants in the *GNB1* gene have been associated with a broad neuropathological phenotype termed GNB1 encephalopathy. We conducted molecular dynamics simulations of the I80T pathological variant that impairs GIRK2 activation to investigate structural and dynamical changes of the $G_{\beta\gamma}$ subunit. The I80T variant was found to have no impact on structure, conformation or dynamics of the isolated $G_{\beta\gamma}$ dimer on the 500 ns time scale. This study shows that the I80T variant is predicted to exert its pathological effect by inducing allosteric changes upon the binding interaction of $G_{\beta\gamma}$ with GIRK2 channel and identifies the need of further experiments to confirm this prediction.

Keywords: GIRK channels, GIRK2, $G_{\beta\gamma}$, I80T variant, mutation, GNB1 encephalopathy, molecular dynamics, structural changes

Zusammenfassung

G-Protein-gekoppelte einwärtsrichtende Kalium (GIRK) Kanäle spielen eine entscheidende Rolle in der hemmenden Neurotransmission, indem sie Neuronen hyperpolarisieren und die elektrische Aktivität von Zellen zum Schweigen bringen. Mutationen führen oft zu einer verminderten Aktivität der GIRK-Kanäle und resultieren in verschiedenen neurologischen Störungen. Missense-Varianten im GNB1-Gen wurden mit einem breiten neuropathologischen Phänotyp namens GNB1-Enzephalopathie in Verbindung gebracht. Wir haben molekulardynamische Simulationen der I80T-pathologischen Variante durchgeführt, die die Aktivierung von GIRK2 beeinträchtigt, um strukturelle und dynamische Veränderungen der $G_{\beta\gamma}$-Untereinheit zu untersuchen. Es wurde festgestellt, dass die I80T-Variante keine Auswirkungen auf Struktur, Konformation oder Dynamik des $G_{\beta\gamma}$-Dimers hat. Diese Studie zeigt, dass die I80T Variante voraussichtlich ihre pathologische Wirkung ausübt, indem sie allosterische Veränderungen bei der Bindungsinteraktion von $G_{\beta\gamma}$ mit dem GIRK2-Kanal induziert, und gleichzeitig identifiziert die Notwendigkeit weiterer Experimente zur Bestätigung dieser Vorhersage.

Schlagwörter: GIRK Kanäle, GIRK2, $G_{\beta\gamma}$, I80T-Variante, Mutation, GNB1-Enzephalopathie, molekulardynamische Simulationen, strukturelle Veränderungen

Table of Contents

List of abbreviations

CTD	cytoplasmic domain
E_K	equilibrium potential
ETX	ethosuximide
GDP	guanosine diphosphate
GIRK (channels)	G protein coupled inwardly rectifying potassium (channels)
GoF	gain of function
GPCR	G protein coupled receptor
GTP	guanosine triphosphate
HBA	hydrogen bond acceptor
HBC	helix bundle crossing
HBD	hydrogen bond donor
Kir (channels)	inwardly rectifying potassium (channels)
LoF	loss of function
MD	molecular dynamics
PIP2	phosphatidylinositol 4,5-bisphosphate
RMSD	root mean square deviation
RMSF	root mean square fluctuation
SASA	solvent accessible surface area
SF	selectivity filter
TMD	transmembrane domain
wt	wild-type

List of tables

List of figures

Introduction

Ion channels are life-essential proteins responsible for maintaining homeostasis and intercellular communication. The inwardly rectifying K^+ channels Kir3.2 that are also referred to as GIRK2 channels are predominantly expressed in neural tissues. Their function is to silence cellular electrical activity, slow synaptic potentials and contribute to the maintenance of cellular resting potential (Lüscher & Slesinger, 2010; Wang *et al.,* 2016). Regulation of GIRK2 channels consists of a complex and not fully understood regulatory interplay between the G protein βγ subunit, PIP_2 and Na^+ ions, where several models of gating mechanisms have been proposed. Albeit the presence of PIP_2 molecules is essential for GIRK2 activation (Li *et al.,* 2019) and Na^+ ions have a regulatory role (Wang *et al.,* 2014), it is debated whether the role of $G_{\beta\gamma}$ is essential or modulatory, while its effect on GIRK2 regulation is substantial (Bernsteiner *et al.,* 2019; Wang *et al.,* 2014).

Mutations are widely recognized as the primary cause of a variety of channelopathies (Kim, 2014). In the recent years, advances of next generation sequencing methods enabled the detection of new disease-causing mutations (Lohmann *et al.,* 2017). GNB1 encephalopathy is a diverse neurodevelopmental condition that often results from mutations in the *GNB1* gene, which encodes the G_β subunit (Reddy *et al.,* 2021). Among patients, the LoF I80T pathogenic variant is the most prevalent, leading to excessive neuronal firing and susceptibility to seizures (Revah-Politi *et al.,* 2020).

The aim of this study was to investigate changes in conformation and dynamics of the $G_{\beta\gamma}$ subunit resulting from the I80T mutation causing GNB1 encephalopathy. MD simulations were employed to model the behavior of wt and mutated $G_{\beta\gamma}$ to test whether the I80T pathological variant influences the stability of $G_{\beta\gamma}$, or whether it exerts its influence on GIRK2 activation through mechanisms of allosteric changes.

1 Literature overview

1.1 Ion channels

Ion channels are life-essential proteins localized in plasma membranes of living cells and their organelles. They play a key role in regulating physiological processes (neuronal signaling, muscle contraction, nutrient transport) and maintaining homeostasis through ion transport. Ion channels form aqueous pores that allow for a highly-selective flow of specific ions (primarily K^+, Na^+, Cl^- or Ca^{2+}) across the lipid bilayer (Rubaiy, 2017).

Ion movement across cell membranes can either be active or passive. While active transport is characterized by movement of ions against the electrochemical gradient and therefore requires additional energy, passive transport takes use of transport along the electrochemical gradient. It is the latter that utilizes conductance, selectivity and gating as key aspects for normal functionality (Rubaiy, 2017).

Ion flow through the channels creates electrical currents that enable for fundamental communication between cells. However, malfunction of normal ion flow gives rise to pathophysiological processes resulting in a multitude of diseases termed channelopathies. The most common cause of channelopathies are mutations, either in genes directly encoding the ion channel, or in their regulatory proteins (Kim, 2014). Therefore, ion channels can serve as therapeutic drug targets for various diseases including neurological disorders such as epilepsy, depression or migraines (Rubaiy, 2017).

1.2 Kir channels

Inwardly rectifying potassium (Kir) channels are transmembrane proteins that possess diverse physiological functions depending on specific subtype and location. They contribute to the maintenance of the cellular resting potential by reducing excitability of neurons and re-establish resting membrane potential in excitable cells. This way they regulate cardiac and neuronal electrical activity, control K^+ transport in non-excitable cells, and transduce communication between the intracellular and extracellular environments (Hibino *et al*., 2010; Lu, 2004). Described in Table 1, based on sequence alignment and phylogenetic analysis, human Kir channels have been classified into 7 subfamilies (Kir1–7) consisting of 16 isoforms characterized by 4 different functional groups and distinct levels of tissue expressions (Cui *et al*., 2021).

Table 1 – Characteristics of Kir family members. The table summarizes similarities and differences among 7 Kir subfamilies in terms of 16 known Kir subunits, functional group specification and expression in various tissues. Intermediate levels of expression are shown in cursive while prominent levels of expression are shown in bold (created according to Cui *et al*., 2021; de Boer *et al*., 2010; Hibino *et al*., 2010).

Kir subfamily	Kir subunits	Functional group	Tissue expression
Kir1.x	Kir1.1	K+ transport channels	*neural*
			kidneys
Kir2.x	Kir2.1, Kir2.2, Kir2.3, Kir2.4, Kir2.6	classical Kir channels	*retina, endothelium/smooth muscle*
			neural, heart, skeletal muscle
Kir 3.x	Kir3.1, Kir3.2, Kir3.3, Kir3.4	G protein-gated K+ channels	*heart, skeletal muscle, kidney, pancreas, endothelium/smooth muscle*
			neural
Kir4.x	Kir4.1, Kir4.2	K+ transport channels	*kidneys*
			neural
Kir5.x	Kir5.1	K+ transport channels	*N/A*
			neural, kidneys, pancreas
Kir6.x	Kir6.1, Kir6.2	ATP-sensitive K+ channels	*neural, heart, skeletal muscle*
			kidneys, pancreas
Kir7.x	Kir7.1	K+ transport channels	*neural, kidneys*
			retina

Kir channel pores consist of 4 subunits, each subunit consists of a transmembrane domain (TMD) and a cytoplasmic domain (CTD). Kir family members show a high sequence similarity of 30–99% allowing for formation of both homomeric and heteromeric assemblies not only within subfamilies (e.g. Kir3.1–Kir3.2), but also across subfamilies (Kir4.1–Kir5.1). Heteromeric formations allow for more unique functional properties in comparison with monomeric structures (Cui *et al*., 2021). Kir channels are generally activated by phosphatidylinositol 4,5-bisphosphate (PIP2), while Kir3.x channels are additionally regulated also by intracellular Na^+ and G protein subunits (Khan *et al.,* 2013; Kurata, 2016). It is Kir3.2 channels that are a focus of this work.

1.2.1 Inward rectification

The key functional feature of Kir channels is to allow for easier movement of K^+ ions in the inward direction rather than in the outward direction. They were first identified in skeletal muscle cells, and due to greater K^+ ion flow into the cell compared to out of the cell, they were initially referred to as "anomalous" rectifier K^+ currents (Hibino *et al*., 2010). Rectification is explained as a change of conductance with voltage, therefore Kir channels are voltage dependent. Kir channels are active at resting membrane potential (around -70 mV), and with an increase in membrane potential (therefore, membrane depolarization), their activity diminishes. Therefore, Kir channels play an important role in the regulation of resting membrane potential (Baronas & Kurata, 2014).

Voltage dependent inward rectification is not an intrinsic property of Kir channels, rather it is a result of asymmetric, open-channel pore blockage by intracellular divalent

cations (Mg^{2+}) or polyamines (Hibino *et al.,* 2010). Upon removal of Kir channels from cellular environments, inward rectification can be reduced or abolished (Lopatin *et al.,* 1994; Lu, 2004).

Under physiological conditions (high intracellular and low extracellular K^+ concentrations), at potentials negative to the equilibrium potential (E_K) of potassium (conditions with no current and no concentration gradient; $E_K \sim -90$ mV), Kir channels allow for a large K^+ current into the cell. On the contrary, at potentials positive to the E_K of potassium, only a small K^+ flux out of the cell is observed due to the binding of polyamines or Mg^{2+} ions (Lüscher & Slesinger, 2010; Rifkin *et al.,* 2017).

At membrane potentials > -90 mV, K^+ ions wish to exit the neuron, while the Kir channel pore is also blocked by polyamines or Mg^{2+} ions. The more positive the membrane potential gets, the tighter the seal of the pore by the blockers gets; however, the blockers do not seal the pore completely and small currents are still possible due to slippage of K^+ ions even at positive potentials. Physiologically, a small outward K^+ flux is present at resting membrane potential (-70 mV). With an increase in membrane potential upon an electrical stimulus (up to ~ +30 mV), K^+ conductance diminishes, therefore Kir channels are not conductive during depolarization and repolarization due to the tighter seal by polyamines and Mg^{2+} ions. With a decrease of membrane potential below -70 mV during hyperpolarization, the seal of the pore by blockers weakens and increased K^+ efflux is observed. At membrane potentials < -90 mV, polyamines and Mg^{2+} ions are to exit the pore, which would enable a rapid K^+ flow into the cell. Physiologically, however, the membrane potential rarely reaches values < -90 mV, therefore rapid inward K^+ currents in Kir channels are uncommon (Baronas & Kurata, 2014; Lu, 2004; Lüscher & Slesinger, 2010). The mechanism is further explained in Figure 1. It is important to mention that not all members of the Kir family show the same degree of rectification, following from strong to weak, where Kir2 > Kir3 >> Kir1 (Glaaser & Slesinger, 2015).

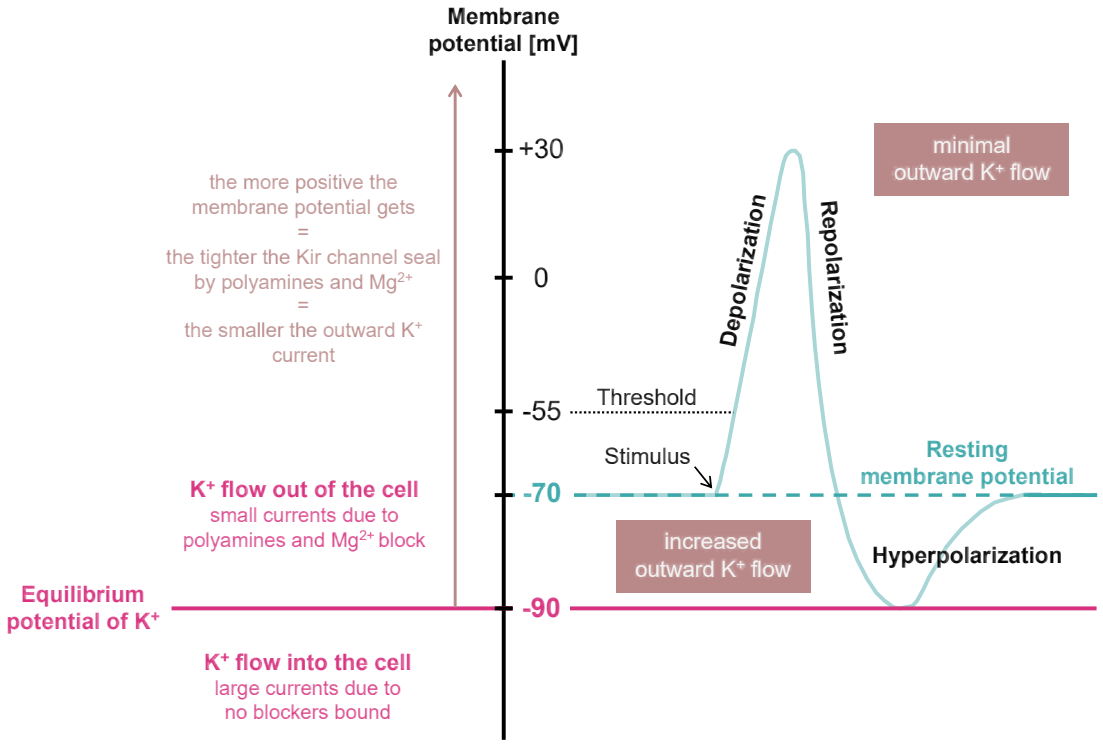

Figure 1 – Schematic mechanism of Kir channel rectification relative to membrane potential. The E_K of K^+ is ~ -90 mV. At membrane potentials > -90 mV, small outward K^+ currents are observed due to the blockage of the pore by polyamines and Mg^{2+} ions. At membrane potentials < -90 mV, polyamines and Mg^{2+} exit the pore, which enables large K^+ inward currents. These are, however, uncommon in physiological environments.

1.3 GIRK channels

G protein-gated K^+ channels, also known as Kir3.x or G protein coupled inwardly rectifying potassium (GIRK) channels, is the only Kir channel subfamily that is directly regulated by G protein subunits and linked to G protein coupled receptors (GPCRs) (Whorton & MacKinnon, 2013). GIRK channels are predominantly expressed in neural tissues (Table 1) and their activity has a crucial role in regulating neurological processes such as pain perception, memory modulation or processes of learning. Moreover, abnormal GIRK function is associated with neural disorders such as epilepsy, anxiety, Parkinson's disease, Down's syndrome, and GNB1 encephalopathy (Jeremic *et al.,* 2021; Lüscher & Slesinger, 2010; Reddy *et al.,* 2021). Similarly, GIRK knockout mice show spontaneous spasms, increased seizure susceptibility or hyperactivity (Lüscher & Slesinger, 2010). Thus, GIRK channels are key for inhibitory neurotransmission in the brain making them valuable targets for development of drugs combating neurological disorders.

1.3.1 GIRK structure

X-ray crystallography and cryo-electron microscopy studies provide for detailed insights into the structure of GIRK channels. There are 4 distinct GIRK channel subunits expressed in mammalian cells: GIRK1 (Kir3.1), GIRK2 (Kir3.2), GIRK3 (Kir3.3) and GIRK4 (Kir3.4). Subunits GIRK1–3 are widely expressed in neural tissues, while expression of GIRK4 is low. In native tissues and heterologous expression systems, GIRK subunits assemble into tetramers to form a functional channel. While GIRK1 and GIRK3 can only form functional channels in heterotetrameric assemblies, GIRK2 and GIRK4 are also functional in homomeric assemblies (Lüscher & Slesinger, 2010). GIRK1–GIRK2 heterotetramers are the predominant form of GIRK channels expressed in the brain (Liao *et al.,* 1996). GIRK-knockout mice studies have revealed that GIRK2 is key for generating GIRK currents in neurons, as mice lacking genes encoding the GIRK2 exhibited little to no GIRK current selected brain regions (Lüscher & Slesinger, 2010). GIRK complexes expressed in mammalian brain are further shown and described in Figure 2.

Figure 2 – GIRK subunit composition in mammalian neuronal cells. GIRK subunits GIRK1, GIRK2 and GIRK3 are widely expressed in the brain, while GIRK4 shows low levels of neural expression (not depicted). GIRK1–GIRK2, GIRK1–GIRK3 and GIRK2–GIRK3 form heterotetramers, while GIRK2–GIRK2 may also form homomers. GIRK1, GIRK2 and GIRK3 subunits can only form heteroterameric channels, they are not functional as homotetramers.

GIRK channels consist of a relatively small TMD and a longer CTD. Each GIRK subunit of the tetramer contains two spinning transmembrane helices, TM1 (outer helix) and TM2 (inner helix). The GIRK N-terminus located in the CTD forms a short loop region that is followed with the TM1 outer helix in the TMD leading to short, extracellular turrets responsible for toxin binding (Glaaser & Slesinger, 2015). A pore helix in the TMD leads to P-loops that form the channel selectivity filter (SF), a narrow pore that discriminates between different ion types and establishes K^+ specificity (Pegan *et al.,* 2005). The sequence motif of the SF is highly conserved among different Kir channels (Tao *et al.,* 2009). P-loops are followed with the TM2 inner helix that transitions into the CTD. GIRK channels contain at least two gates that undergo a conformational change: a helix bundle

crossing (HBC) gate located in the lower part of the TMD close to the inner leaflet of the membrane bilayer, and a G-loop gate in the apex of the CTD. These regions are responsible for either allowing or preventing K^+ ions to move through the channel, influencing K^+ conductivity. HBC and G-loop gates are regulated by the binding of the $G_{\beta\gamma}$ protein subunit, PIP_2 molecules and Na^+ ions, the gating mechanism is further described in Chapter 1.3.3 (Friesacher *et al.,* 2022; Li *et al.,* 2018; Pegan *et al.,* 2005). The $G_{\beta\gamma}$ protein subunit binds to the GIRK channel in the CTD while the Gγ C-terminus functions as an anchor to the membrane (Whorton & MacKinnon, 2013). It is important to mention that available structures often lack several amino acids at the N and C-termini and are considered intrinsically disordered (Pegan *et al.,* 2005). The structure of a GIRK2–$G_{\beta\gamma}$ complex and its regulators is depicted in Figure 3.

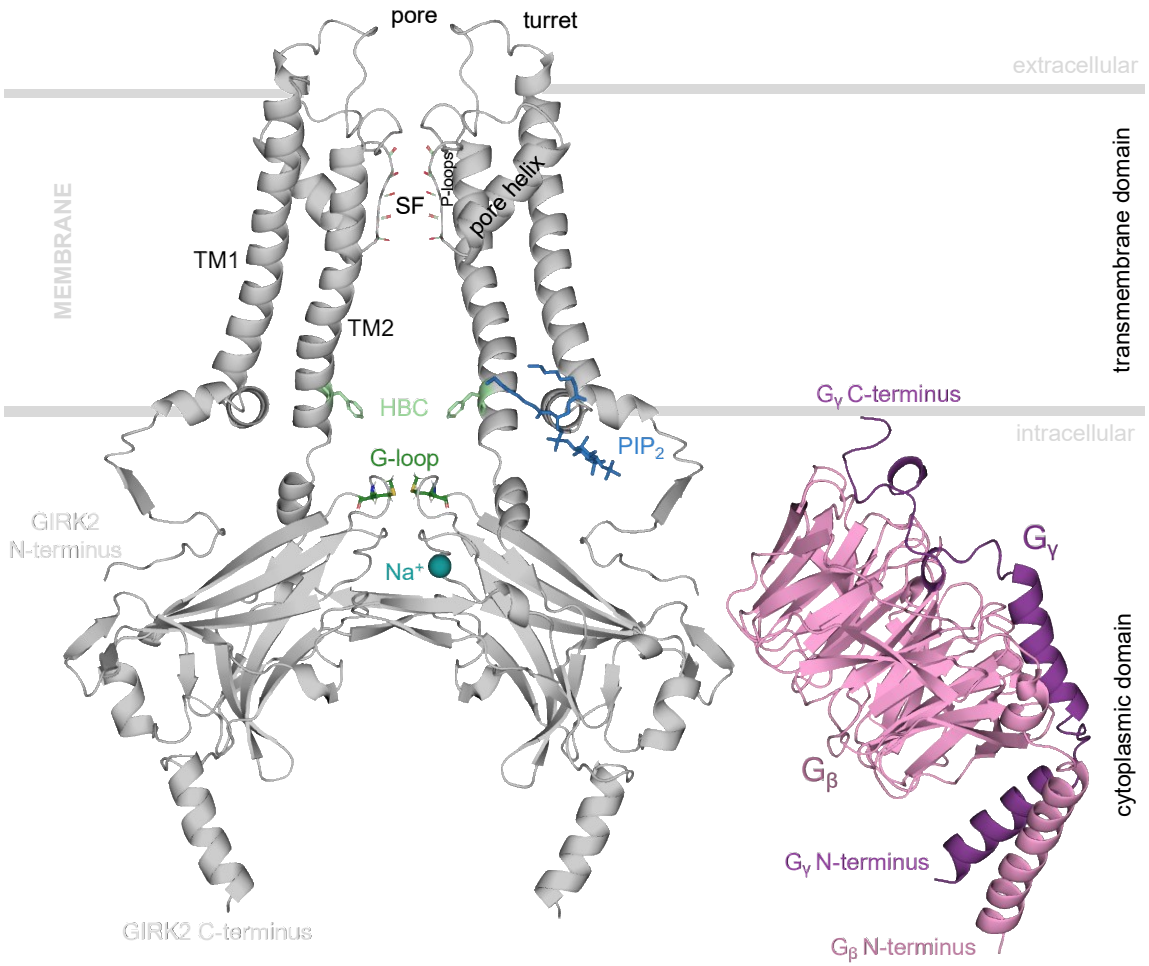

Figure 3 – Structure of the GIRK2–$G_{\beta\gamma}$ complex and its regulators (PDB: 4KFM). Two opposing dimers are displayed and only one $G_{\beta\gamma}$ protein subunit is shown for clarity. The approximate membrane extent is shown with gray lines indicating the transmembrane and cytoplasmic domain of the channel. GIRK2 is shown in gray, G_β in pink and G_γ in purple. The HBC and G-loop gate are shown in green. Bound Na^+ ions are represented as teal spheres and PIP_2 is shown in blue. On each GIRK2 homotetramer, there are 4 binding sites for each regulating ligand: $G_{\beta\gamma}$, PIP_2 and Na^+.

1.3.1.1 4KFM structure model

The 4KFM model (Whorton & MacKinnon, 2013) with a resolution of 3.45 Å presents a crystal structure of the mammalian (mouse) GIRK2 channel bound in complex with the $G_{\beta\gamma}$ protein subunits in a tetrameric formation. This signaling complex is a central link between GPCR stimulation and Kir channel activity (Whorton & MacKinnon, 2013).

As hydrated K^+ ions are 8 Å in diameter, the pore of open GIRK2 channels is required to be greater in order to allow passage of K^+ ions. Hydrophilic pore of the constitutively open GIRK2 R201A mutant was measured to be 9 Å in diameter, sufficiently allowing passage of hydrated K^+ ions (Whorton & MacKinnon, 2011). Similarly, other constitutively open K^+ channels have a pore diameter of 10 Å. As the pore diameter of GIRK2 in the 4KFM structure is only 6–7 Å, the authors suggest a pre-opened state of GIRK2, where four $G_{\beta\gamma}$ subunits are stabilized at the interfaces between four identical GIRK2 channel subunits by short-range atomic and long-range electrostatic interactions (Whorton & MacKinnon, 2013).

The binding of $G_{\beta\gamma}$ to GIRK2 subunits results in a rotation of the CTDs with respect to TMDs and splaying of the TM2 helices, accounting for the intermediate pre-open conformation between opened and closed state of the constitutively active channel. GIRK2 channels in the pre-open state exhibit so-called burst kinetics, when the $G_{\beta\gamma}$ activated GIRK2 channel is believed to flicker rapidly between conductive (open) and non-conductive (pre-open) conformations (Whorton & MacKinnon, 2013). The 4KFM model is the only available structure of GIRK2 co-crystallized with $G_{\beta\gamma}$.

1.3.2 G protein function and structure

G proteins are essential components of downstream signal transduction pathways. GPCRs are plasma membrane receptors that are crucial for physiological functioning of vital systems in the organism. In an inactive state, G proteins are bound to GPCRs as heterotrimers consisting of subunits G_α, G_β and G_γ. Several structurally different forms of each monomer (α, β and γ) are identified in humans, which allows for creation of various distinct heterotrimeric complexes that determine specificity for effector molecules. Upon GPCR activation by agonists, the G_α subunit dissociates from the $G_{\beta\gamma}$ and $G_{\beta\gamma}$ acts as a key GIRK2 modulator (Duc *et al.,* 2015).

The G_α protein subunit is composed of a Ras-like domain and α-helical domain, between which the nucleotide-binding pocket is located. The Ras-like domain provides

a binding site for the $G_{\beta\gamma}$ subunits and has a slow GTPase activity to hydrolyze guanosine triphosphate (GTP) into guanosine diphosphate (GDP) after activation (Duc *et al.,* 2015).

The $G_{\beta\gamma}$ subunit directly interacts with GIRK2 through G_{β} binding to the CTD, while the C-terminus of G_{γ} covalently anchors the complex to the membrane through the prenylated lipid tail (Whorton & MacKinnon, 2013). Prenylation is a type of lipid modification characterized by the addition of 20-carbon geranylgeranyl isoprenoids to conserved cysteine residues at the C-terminus (Zhang & Casey, 1996). The $G_{\beta\gamma}$ is a dimer composed of two polypeptides that never dissociate in physiological environments. They are held together primarily by hydrophobic interactions, and are therefore seen as one functional unit (Higgins & Casey, 1994). The G_{γ} subunit is vital for proper expression and folding of the G_{β} subunit that belongs to the β-propeller family of proteins (Schmidt *et al.,* 1992). The N-terminal helices of both subunits form a coiled-coil interaction that stabilizes the complex with respect to the 7 antiparallel β-sheets of G_{β} (Sondek *et al.,* 1996).

The hydrophobic contact interface between GIRK2 and $G_{\beta\gamma}$ dimer is approximately 700 Å and mediated through short-range hydrogen bonds and long-range electrostatic interactions (Whorton & MacKinnon, 2013). The binding site occurs at the interface of two adjacent GIRK2 subunits, where each of the $G_{\beta\gamma}$ subunits binds to the CTDs of both channel subunits. A set of amino acids unique to GIRK2–$G_{\beta\gamma}$ binding site has been identified and includes residues Gln248 and Phe254 of one GIRK2 subunit interacting with residues Gln75, Ser98 and Trp99 of G_{β}, and the sequence Leu-Thr/Ser-Leu (342–344) of the adjacent GIRK2 subunit forming contacts with residues Leu55 and Lys78 of G_{β} (Whorton & MacKinnon, 2013). The GIRK2–$G_{\beta\gamma}$ binding interface is shown in Figure 4, however, it is of importance to note that it has not been fully deciphered yet.

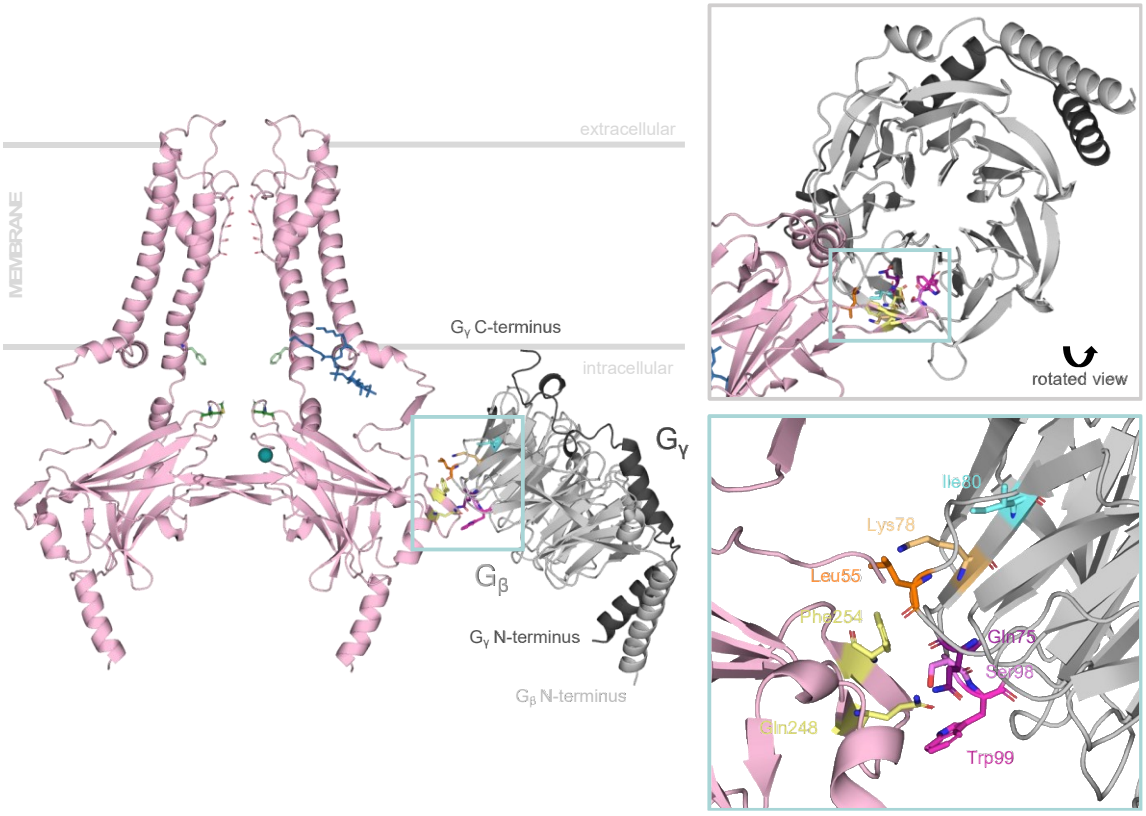

Figure 4 – Structure of the GIRK2–$G_{\beta\gamma}$ complex binding interface (PDB: 4KFM). Two opposing dimers of GIRK2 are displayed and only one $G_{\beta\gamma}$ subunit is shown for clarity. Interacting residues of one GIRK2 subunit Gln248 and Phe254 are shown in yellow, these form hydrogen bonds with residues Gln75, Ser98 and Trp99 of G_β shown in shades of purple. Leu55 and Lys78 of G_β shown in orange would interact with the adjacent GIRK2 subunit that is not shown for clarity. Ile80 is not located directly in the binding site, but is shown to demonstrate its binding site proximity, as residue 80 is a focus of this work.

1.3.3 GIRK2 gating mechanism

As GIRK2 channels have been shown to play important roles in both physiological (memory, learning) and pathophysiological (drug addiction, epilepsy, Parkinson's disease, Down's syndrome) neurological processes, elucidation of their gating mechanism has gained a lot of interest in order to develop drugs that successfully target GIRKs (Jeremic *et al.,* 2021). As previously mentioned, K^+ ions have to overcome 3 constrictions in order to permeate through GIRK2 channels: the SF, the HBC gate and the G-loop gate. Electrophysiological and structural studies along with planar bilayer experiments have shown that PIP_2 molecules must be present for channel activation while Na^+ ions are not essential, but further promote channel opening (Wang *et al.,* 2014). It is still debated whether the presence of $G_{\beta\gamma}$ subunits is essential for GIRK2 activation (Bernsteiner *et al.,* 2019; Wang *et al.,* 2014). Binding of $G_{\beta\gamma}$ subunits, PIP_2 and Na^+ ions in close proximity to the gates results in conformational changes of the pore that opens wide enough to allow K^+ ions to pass through the channel (Bernsteiner *et al.,* 2019; Pegan *et al.,* 2005).

However, GIRK2 gating regulation by multiple intracellular regulators is a complex mechanism that is not fully understood and has yet to be decoded in detail. Several models of the regulatory interplay between $G_{\beta\gamma}$, PIP_2 and Na^+ have been proposed and despite being partially contradictory, they all indicate that GIRK2 regulators act through a complicated, allosteric network inducing a multitude of conformational changes of the channel and its gates (Li *et al.,* 2019; Niu *et al.,* 2020; Wang *et al.,* 2016). Reconstitution experiments have shown that the individual regulators can activate the channel partially, but in combination, they act synergistically and activate it to a greater extent (Whorton & MacKinnon, 2013). However, the details of how the GIRK2 gates are controlled by $G_{\beta\gamma}$, PIP_2 and Na^+ still need to be elucidated.

1.3.3.1 $G_{\beta\gamma}$ activation

GIRK2 channels in the brain can be activated by various inhibitory neurotransmitters (including serotonin, dopamine, somatostatin, opioids and gamma-aminobutyric acid) through GPCRs (Glaaser & Slesinger, 2015). In the absence of a receptor agonist, the GPCR is bound to the G protein in an inactive state. The G protein is a trimer, where the G_α subunit binds GDP and forms a complex with $G_{\beta\gamma}$. When an agonist stimulates the GPCR and activates it, the GTPase activity of G_α increases, converting bound GDP into GTP, which induces the dissociation of the heterotrimeric G protein from the receptor that further dissociates into G_α and $G_{\beta\gamma}$. The G_α subunit remains attached to the membrane via its N-terminus and further interacts with various effector molecules (Duc *et al.,* 2015; Hibino *et al.,* 2010). The $G_{\beta\gamma}$ subunit is believed to activate the GIRK2 channel in a membrane delimited phenomenon, where the $G_{\beta\gamma}$ diffuses towards the channel, while it is still attached to membrane's cytoplasmic surface. The $G_{\beta\gamma}$ subunit then attaches to GIRK2 via the interaction of G_β with the channel CTD and the G_γ prenylated C-terminus ensures membrane attachment (Whorton & MacKinnon, 2013). A study of computational modeling and MD simulations has determined that $G_{\beta\gamma}$ stabilizes the HBC gate in an open state via inducing a rotation/tilt of the CTD (Li *et al.,* 2019). The influence of $G_{\beta\gamma}$ on the activation of GIRK2 is further described in Figure 5.

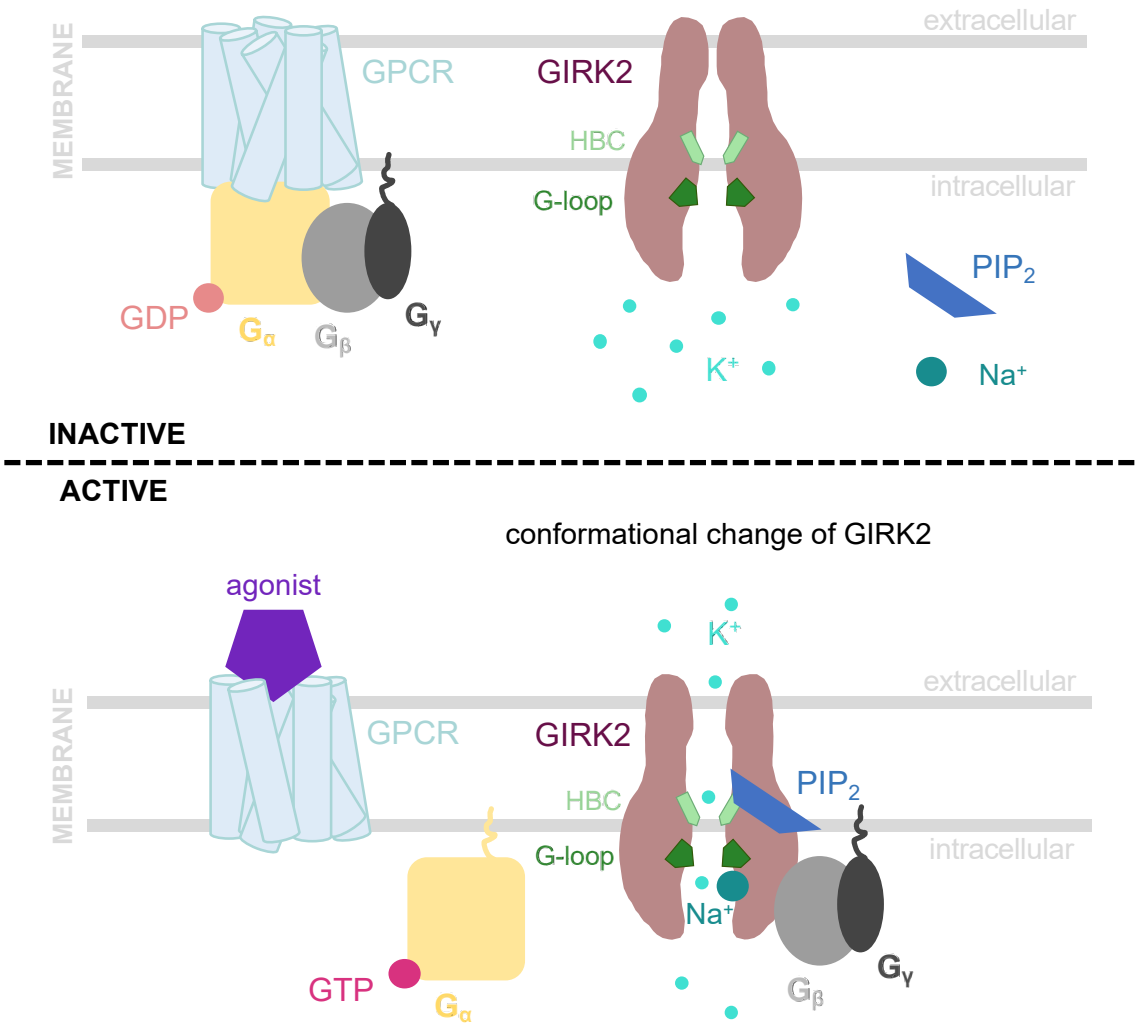

Figure 5 – Gating mechanism of GIRK2 channel activation. In an inactive state in the absence of a GPCR agonist, a trimeric G protein bound to GDP is attached to GPCR. Upon agonist binding to the GPCR, a GDP/GTP exchange is accelerated on a bound G protein, which induces G protein dissociation. The $G_{\beta\gamma}$ subunit then binds to the CTD of GIRK2, and in the presence of PIP_2 and Na^+ induces conformational changes of the HBC and G-loop gates causing the channel to open and K^+ ions permeate through. The approximate membrane extent is shown with gray lines indicating the transmembrane and cytoplasmic domain of the channel. GPCR is represented in light blue, GPCR agonist in purple, GIRK2 channel in burgundy, HBC and G-loop gates in shades of green. GDP and GTP are depicted in shades of pink. G_α subunit is depicted in yellow and $G_{\beta\gamma}$ in shades of dark grey. PIP_2 is shown in blue, K^+ ions in turquoise and Na^+ ions in teal.

In the presence of membranes that contain PIP_2 molecules, $G_{\beta\gamma}$ has been shown to be sufficient to increase the open probability of GIRK2 channels. However, it is not known how many $G_{\beta\gamma}$ subunits are needed to open the channel (Whorton & MacKinnon 2013). As the G_α and GIRK2 binding sites with $G_{\beta\gamma}$ overlap, GPCR activation and the dissociation of heterotrimeric G protein into G_α and $G_{\beta\gamma}$ is required for GIRK2 activation, but whether a single GPCR in close proximity to the channel is sufficient to activate the channel, or whether multiple receptors are required still remains a question (Whorton & MacKinnon, 2013).

Dissociation of $G_{\beta\gamma}$ from GIRK2 is not well studied and it is not clear how long does it stay bound to the channel and which influencing factors are key. However, the hydrolysis of GTP into GDP (due to the slow GTPase activity of G_{α}) reverts the conformational change of the G protein. This mediates the separation of $G_{\beta\gamma}$ from GIRK2 and causes channel deactivation (Jeremic *et al.,* 2021). The G_{α} subunit is likely to indirectly deactivate GIRK2 channels by binding the free, channel unbound $G_{\beta\gamma}$ subunits and shifting the $G_{\beta\gamma}$ equilibrium away from channel occupancy (Wang *et al.,* 2014).

1.3.3.2 The role of Na^+

Sodium enters neurons during the firing of action potentials, therefore the concentration of intracellular Na^+ increases during excessive electrical excitation. Na^+ ions bind to the CTD of GIRK2 below PIP_2 and below the G-loop gate. Multiple groups have hypothesized that the presence of Na^+ ions increases the binding affinity of PIP_2 to GIRK2 channel. Therefore, Na^+ is not essential and not sufficient for channel activation, but it modulates the effect of PIP_2 and $G_{\beta\gamma}$ over physiological concentrations (Huang *et al.,* 1998; Wang *et al.,* 2014; Wang *et al.,* 2016). A study of computational modeling and MD simulations has determined that Na^+ ions control the G-loop gate and stabilize it in an open state through inducing an anti-clockwise rotation (Li *et al.,* 2019). Therefore, increased intracellular concentration of Na^+ ions appears to help in activation of GIRK2 channels through conformational control of gating mechanisms (Figure 5).

1.3.3.3 PIP_2 requirement

Activation of GIRK2 channels is dependent on the presence of PIP_2 molecules that stabilize the HBC and G-loop gates in an open state through direct interactions (Li *et al.,* 2019). PIP_2 is a signaling lipid that binds to GIRK2 in close proximity of the HBC gate located in the CTD-TMD interface. PIP_2 acts as an allosteric regulator to permit $G_{\beta\gamma}$ binding to GIRK2 by reshaping the $G_{\beta\gamma}$ binding surface on the CTD (Niu *et al.,* 2020). The exact role of PIP_2 is enigmatic, though based on cryo-electron microscopy analysis of PIP_2 regulation, it has been hypothesized that PIP_2 brings the CTD of the channel closer to the membrane surface. As $G_{\beta\gamma}$ is held at the membrane surface through the geranylgeranyl lipid tail on the G_{γ} C-terminus, bringing the CTD closer to membrane surface could be a key event in order for $G_{\beta\gamma}$ to bind. In the absence of PIP_2, $G_{\beta\gamma}$ is therefore unable to bind to the channel, as it cannot access its binding site on GIRK2 (Figure 5) (Li *et al.,* 2019; Niu *et al.,* 2020). Additionally, PIP_2 on its own is not able to gate

the GIRK2 channel efficiently, and the presence of $G_{\beta\gamma}$ subunits and Na^+ ions has shown to increase the affinity of GIRK2 to PIP_2 in synergistic mechanisms (Logothetis *et al.,* 2015).

1.3.4 GIRK pathology

As previously mentioned, GIRK malfunctions are implicated in the pathophysiology of a multitude of channelopathies, with mutations being their most prominent cause. Two genetical pathological principles are distinguished: gain of function (GoF) or loss of function (LoF) mutations. GoF mutations of GIRK channels show increased ionic currents and can considerably reduce neural activity through silencing neuronal firing, such is implicated in Down's syndrome. On the other hand, LoF GIRK mutations show decreased ionic currents and lead to excessive neuronal excitability, increased firing and susceptibility to seizures, as observed in epilepsy or GNB1 encephalopathy. Additionally, loss of selectivity across GIRK channels can cause aberrant, constitutively active K^+ outward fluxes that trigger cell death that is implicated in the pathology of Parkinson's disease (Lüscher & Slesinger, 2010; Mathiharan *et al.,* 2021; Reddy *et al.,* 2021).

Several specific mutations on the GIRK2 channel and on the G protein were shown to alter the GPCR mediated activation of channels, often causing problematic binding of $G_{\beta\gamma}$ to GIRK2 (Whorton & MacKinnon, 2013). This work focuses on the I80T LoF mutation of the G_β subunit that causes GNB1 encephalopathy (Reddy *et al.,* 2021).

1.4 GNB1 encephalopathy

Even though the complex etiology of most neurodevelopmental syndromes is not elucidated, the unraveling of genetic causes is rapidly increasing and hundreds of new genes and their mutations are being implicated as disease-causing. Among these, the *GNB1* gene encoding for the $G_{\beta1}$ subunit of G protein has recently been described as causal for a heterogeneous neurodevelopmental syndrome termed GNB1 encephalopathy, also known as GNB1 syndrome, in which a unifying characteristic is global development delay present in 100% of patients (Da Silva *et al.,* 2021; Hemati *et al.,* 2018; Revah-Politi *et al.,* 2020).

1.4.1 Manifestations

GNB1 encephalopathy is a genetically determined neurological disorder that is characterized by moderate to severe developmental delay and/or intellectual disability, seizures, epileptiform activity in the electroencephalogram, structural brain abnormalities and muscle hypotonia. Additional symptoms that vary among patients may include dystonia (involuntary muscle contractions), growth delay, behavioral issues, reduced vision, gastrointestinal problems, genitourinary problems in males and cutaneous mastocytosis. Disease management includes symptomatic treatment of above listed manifestations as per standard care (Revah-Politi *et al.,* 2020).

1.4.2 Prevalence

GNB1 encephalopathy is a rare disease with less than 100 confirmed cases worldwide (as of October 23rd 2023, 64 cases are known), where no increased disease prevalence has been shown in specific ethnic groups or populations. However, due to the small number of patients reported, clinical data is limited. As the mutations causing GNB1 encephalopathy have only been discovered recently and diagnosis tools are not widely available due to high costs, it is expected that many patients have been previously misdiagnosed with for example autism spectrum disorders, cerebral palsy, or epilepsy-associated developmental delays (Revah-Politi *et al.,* 2020; www1).

1.4.3 Prognosis

Life expectancy and common causes of death are unknown, as most of the patients reported are children or young adults. As many adult patients with intellectual disabilities have not undergone advanced genetic testing, it is expected that adult GNB1 encephalopathy patients are misdiagnosed, and therefore under-reported. Due to the absence of high morbidity or mortality congenital anomalies, it is believed that with appropriate management of symptoms, the prognosis for patients appears favourable (Revah-Politi *et al.,* 2020).

1.4.4 Diagnosis

Up to half of children suffering from severe developmental disorders of probable genetic origin remain without an official genetic diagnosis despite the rapid progression of diagnostic tools in the last decades. Diagnostics of rare disorders with variable clinical

manifestations is particularly challenging, as it is difficult to distinguish them from other, clinically indistinguishable disorders (Fitzgerald *et al.,* 2015). Formal diagnostic criteria for GNB1 encephalopathy have not yet been established and the disease should be considered in patients that present with its manifestations. However, given the fact that phenotypic features associated with GNB1 encephalopathy are insufficient and associated with other diseases, it is difficult to suspect the disease solely based on clinical features. The diagnosis is confirmed by molecular genetic testing through identification of a heterozygous *GNB1* pathogenic variant (Revah-Politi *et al.,* 2020).

Whole-exome sequencing studies on patients presenting with a set of relatively unspecific clinical features have recently been proven as a powerful strategy in discovering disease-associated genes and identifying de novo mutations in affected populations. Clinical sequencing labs report that among the individuals recruited for undiagnosed genetic disorders, around a third of them are diagnosed following whole-exome sequencing, with de novo pathogenic variants being the most prominent cause (Petrovski *et al.,* 2016).

1.5 GNB1 genetics

The *GNB1* gene (chromosome locus 1p36.33) encodes the $G_{\beta 1}$ subunit of the heterotrimeric G protein (Reddy *et al.,* 2021). Functional studies have shown that abnormal $G_{\beta 1}$ impairs the function of the G protein (Lohmann *et al.,* 2017). The disease is most often caused by a de novo *GNB1* pathogenic variant resulting from a germline missense mutation, but rarely can also be caused by deletions, splice site mutations, or inherited from parents to offspring in autosomal dominant manner. Penetrance is expected to be 100% (Da Silva *et al.,* 2021; Revah-Politi *et al.,* 2020). The disease phenotype associated with de novo missense *GNB1* pathogenic variants was first described by Petrovski *et al.* in 2016 (Hemati *et al.,* 2018).

1.5.1 GNB1 pathogenic variants

So far, around 30 different missense variants have been reported, with I80T being the most abundant and recurrent variant among patients (Revah-Politi *et al.,* 2020). As the *GNB1* gene is naturally highly intolerant to genetic variation in general population, the identification of multiple de novo missense mutations is remarkable. Moreover, the GNB1 protein is extremely well conserved among humans and other mammals,

demonstrating that as no mutations were selected during evolution, any arisen mutation could have structural impact (Da Silva *et al.,* 2021). By the means of estimating the mutation rate in genes and then comparing it to the observed *GNB1* mutation rate, *GNB1* is securely implicated as a genome-wide-significant disease-associated gene (Petrovski *et al.,* 2016).

The majority (88%) of the pathogenic missense variants identified so far are located in exons 6 and 7 of the *GNB1* gene that encode the residues 76 – 118. These regions represent only 12.6% of the total *GNB1* coding sequence, indicating the presence of a mutational hotspot. Encoding for majority of residues important for generating the interaction between G_{α} and $G_{\beta\gamma}$, exons 6 and 7 are implicated to be of particular importance, as mutations in these are likely to compromise proper binding of G protein subunits (Da Silva *et al.,* 2021; Hemati *et al.,* 2018). Notable *GNB1* missense pathogenic variants are selected and briefly described in Table 2. A list of additional *GNB1* pathogenic variants can be found in a Case Report published by Da Silva *et al.* in 2021.

Table 2 – Notable *GNB1* pathogenic missense variants. The table lists selected notable pathogenic missense variants of the *GNB1* gene that are associated with neurodevelopmental delay.

DNA nucleotide change	Protein change		GoF/LoF mutation	Reference
c.158 G>A	p.Gly53Glu	G53E	?	Hemati *et al.*,2018
c.229 G>C	p.Gly77Arg	G77R	?	Hemati *et al.*,2018
c.233 A>G	p.Lys78Arg	K78R	GoF	Petrovski *et al.*,2016; Reddy *et al.*,2021
c.239 T>C	p.Ile80Thr	I80T	LoF	Petrovski *et al.*,2016; Reddy *et al.*,2021
c.239 T>A	p.Ile80Asn	I80N	GoF	Petrovski *et al.*,2016; Reddy *et al.*,2021
c.266 A>G	p.Lys89Arg	K89R	?	Hemati *et al.*,2018
c.275 C>A	p.Ala92Asp	A92D	?	Hemati *et al.*,2018
c.284 T>C	p.Leu95Pro	L95P	LoF*	Petrovski *et al.*,2016
c.287 G>T	p.Arg96Leu	R96L	LoF	Lohmann *et al.*,2017
c.301 A>G	p.Met101Val	M101V	LoF*	Petrovski *et al.*,2016
c.341 G>A	p.Cys114Tyr	C114Y	?	Hemati *et al.*,2018
c.352 G>T	p.Asp118Tyr	D118Y	GoF	Jones *et al.*,2019
c.353 A>G	p.Asp118Gly	D118G	LoF	Firth *et al.*,2009; Hemati *et al.*,2018

* supported by preliminary experimental data of our collaborator Nathan Dascal, Tel Aviv University

1.5.1.1 I80T variant

Being the most commonly reported variant identified in 20–25% of GNB1 encephalopathy patients, the G_{β} I80T missense mutation gains a lot of interest in the scientific community (Da Silva *et al.,* 2021; Revah-Politi *et al.,* 2020). Residue 80 is not located directly in the GIRK2–$G_{\beta\gamma}$ binding interface, but lies in its close proximity (see Figure 4). Therefore, we aim to investigate how the I80T pathogenic variant impacts the structure and dynamics of $G_{\beta\gamma}$. The I80T variant carries a LoF missense point mutation, in which thymine is substituted with cytosine on the nucleotide position 239, resulting in the change of isoleucine into threonine of the amino acid on position 80. While isoleucine is a more hydrophobic residue due to the presence of an ethyl side chain, its interactions with surrounding residues are limited to hydrophobic contacts. On the other hand, threonine is more active due to its more hydrophilic nature and presence of an additional OH functional group that can function as a hydrogen bond acceptor (HBA) or hydrogen bond donor (HBD), and therefore interact with surrounding residues via hydrogen bonds (Petrovski *et al.,* 2016; Reddy *et al.,* 2021) (Figure 6).

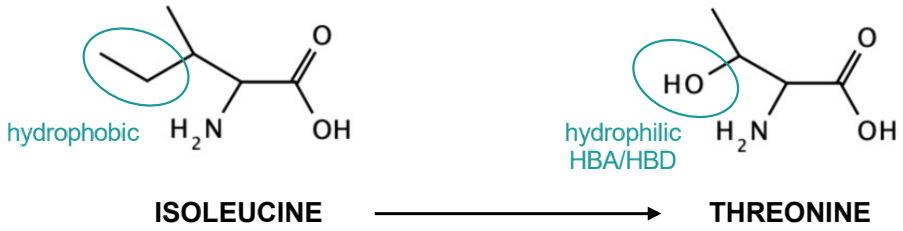

Figure 6 – Structure of isoleucine and threonine. The I80T pathogenic variant is characterized by the change of isoleucine into threonine on amino acid level. The change on an atomistic level is circled in blue. While isoleucine is a more hydrophobic residue due to its ethyl side chain, threonine is more hydrophilic, as it contains an additional OH functional group that acts as a HBA or HBD.

1.5.1.1.1 Mechanisms of I80T mutation-induced changes in $G_{\beta\gamma}$ action on GIRK2

So far, information regarding functional changes on the molecular level caused by pathological *GNB1* variants has been limited. The mechanism of mutation-induced changes in $G_{\beta\gamma}$ action on GIRK2 including the I80T variant was first described by Reddy *et al.* in 2021. They found that mutations (GoF K78R, LoF I80N and LoF I80T) have an effect on the $G_{\beta\gamma}$ regulation of GIRK2 channels while they also observed changes in protein expression levels (Reddy *et al.,* 2021).

In the past, loss of expression patterns was often observed in missense variants for a variety of proteins. For the I80N and I80T variants, partial loss of $G_{\beta\gamma}$ expression has been shown. However, both the I80N/T variants failed to activate GIRK2 homomeric

channels even when the mutated $G_{\beta\gamma}$ was overexpressed in comparison with wild-type (wt) $G_{\beta\gamma}$, indicating that the partial loss of expression is not a key factor. However, GIRK1/2 heteromeric channels were activated by the I80N/T $G_{\beta\gamma}$ variants in the same manner as with wt $G_{\beta\gamma}$, confirming that surface expression and functionality of I80N/T $G_{\beta\gamma}$ is sufficient and suggesting a strong LoF effect towards GIRK2 homomers. Therefore, the LoF effect is GIRK-subunit specific. The changes in I80N/T $G_{\beta\gamma}$ binding to the CTD of GIRK2 were mild, suggesting that diminished channel activation could also be due to deficiencies in gating (Reddy *et al.,* 2021).

The decrease of I80N/T $G_{\beta\gamma}$ binding to GIRK2 channels suggests the importance of residue 80 in the interaction. However, as I80 is not part of the GIRK2-$G_{\beta\gamma}$ interface, the question whether the mutation could allosterically affect GIRK2-$G_{\beta\gamma}$ interplay arises (Reddy *et al.,* 2021). It is important to test whether the I80T mutation influences the stability of $G_{\beta\gamma}$, and therefore the activation of GIRK2 allosterically. We propose that allosteric changes in the $G_{\beta\gamma}$ subunit caused by the I80T mutation could prevent the activation of GIRK2.

1.6 MD simulations

Throughout the last decades, *in silico* methods and computer-aided drug design have come to the forefront of pharmaceutical research (Bassani & Moro, 2023). Due to the rapid advancement of computational power and recent breakthroughs in crystallographic methods, the impact of MD simulations has expanded dramatically, most notably in the fields of molecular biology and drug discovery (Hollingsworth & Dror, 2018). As protein structures are often not sufficient to predict the function and movement of complex molecular structures, MD simulations are a commonly used tool to investigate and predict the dynamical properties of molecules in full atomic detail and high resolution (De Vivo *et al.,* 2016; Hollingsworth & Dror, 2018).

1.6.1 Basic principles

Based on the principles of physics, MD simulations predict the movement of every single atom in a protein over time with respect to interatomic interactions (Karplus & McCammon, 2002). Initial coordinates of the protein atoms can be obtained with experimental structural biology techniques, such as X-ray crystallography or cryo-electron microscopy. A mechanical force field is used to calculate potential energies and forces

acting upon all atoms of the system to predict the dynamics of the system. The trajectory of atoms specifying their positions and velocities is then obtained based on solving Newtonian equations of motion as a function of time, generating successive configurations of the moving system. Obtaining MD simulations is therefore an iterative process, in which predicted new positions of all atoms of the system are established, resulting in a substantial number of snapshots describing the evolvement of the system over the course of the simulation (Adcock & McCammon, 2006; De Vivo *et al.,* 2016; Hollingsworth & Dror, 2018).

1.6.2 Advantages and limitations

MD simulations are a powerful tool to gain detailed insights into molecular systems on an atomistic level, which is highly convenient for elucidating molecular mechanisms. In comparison with laboratory experimental techniques, MD simulations allow for a high control over the conditions of the experiment, and therefore the investigation of the behavior of molecules under a set of very specific conditions. Additionally, as MD simulations capture the positions of all atoms at every point in time, they allow for visualization of molecular behavior at the atomic level, which is difficult to achieve and replicate in the laboratory (Hollingsworth & Dror, 2018). With the advancement of graphical processing units and user-friendly software codes, MD simulations are becoming more accessible and affordable with a possibility to run simulations not only in the frame of nano and microseconds, but also milliseconds (De Vivo *et al.,* 2016).

However, the requirements for computational power are still high. This can limit the size of the simulated system, as well as the length of the simulation. Routinely performed MD simulations are normally on the microsecond time scale due to high computing times, often leading to insufficient sampling of conformational states. Furthermore, biological processes, such as ligand binding or large-scale conformational changes, might take too long to be observable in MD simulations. As the force field parameters used to obtain the trajectory are only approximations of the quantum-mechanical reality, the question of limitations to accuracy arises, and the results of MD simulations must ultimately be verified by laboratory experiments (Durrant & McCammon, 2011).

MD simulations are a valuable tool to be used in combination with wet-lab experiments and despite their higher initial cost into computing hardware, simulations can lower resources on the long-run and provide for a faster, more efficient research (Hollingsworth & Dror, 2018).

1.6.3 Indication

MD simulations have been proven to be valuable in elucidating molecular and functional mechanisms of biomolecules helping to uncover structural basis for disease pathophysiology, and are commonly used in the prediction of severity of disease-associated mutations (Reddy *et al.,* 2021). A trend particularly noticeable in neuroscience is that MD simulations are increasingly being used in experimental structural biology studies to help interpret experimental results and further guide experiments critical to neuronal signaling (Hollingsworth & Dror, 2018). Even though the accuracy of physical models underlying MD simulations is substantially increasing, it is important to keep in mind they are inherently approximations, uncertainty should be considered when analyzing simulations and the results should be further confirmed by the means of wet-lab experimental data (Hollingsworth & Dror, 2018; Reddy *et al.,* 2021).

2 Objective

The objective of the master thesis was to investigate structural changes of the $G_{\beta\gamma}$ subunit caused by I80T LoF mutation associated with GNB1 encephalopathy. Since I80T has been shown to alter GIRK activation (Reddy *et al.,* 2021), our findings of mutation-associated structural changes of $G_{\beta\gamma}$ could shed new insights into the complicated network of GIRK channel regulation by G protein and PIP_2. We propose that the I80T mutation located in close proximity of the binding interface causes allosteric changes (stability, compactness, conformation, dynamics) of the $G_{\beta\gamma}$ subunit which could prevent the activation of GIRK2 channels. To achieve the objective of this work, we took the following steps:

- Conducted MD simulations of unbound wt and I80T mutant in solution to evaluate the effect of pathological variant on conformational flexibility of $G_{\beta\gamma}$.
- Compared MD simulations of unbound wt $G_{\beta\gamma}$ with previously conducted simulations of GIRK2 bound wt $G_{\beta\gamma}$ to ensure structural uniformity of bound and unbound $G_{\beta\gamma}$.
- Analyzed $G_{\beta\gamma}$ trajectories and structural changes through calculations of selected descriptive parameters.

3 Materials and Methods

3.1 Structure

The starting structure of the GIRK2 $G_{\beta\gamma}$ subunit for MD simulations was obtained from a crystal structure of the GIRK2 (Kir3.2) in complex with the $G_{\beta\gamma}$ subunits (PDB accession #4KFM, resolution 3.45 Å) (Whorton & MacKinnon, 2013). For the wt and I80T simulations, the $G_{\beta\gamma}$ subunit was remodeled and generated in SwissPDBViewer, missing side chain residues were added (Guex & Peitsch, 1997). For the simulations of GIRK2 bound $G_{\beta\gamma}$, the full 4KFM structure was used; the simulations were provided by Theres Friesacher, BSc MSc.

3.2 System preparation

For the wt and I80T MD simulations, the solvated, electroneutral system was configured in the Solution Builder (formerly known as Solvator) provided by CHARMM-GUI webserver (accessed April 27th, 2023) (Jo *et al.,* 2008). A rectangular water box was selected, its size was fitted to protein size with an edge distance of 12 Å. The simulation box was solvated according to the TIP3P water model (Jorgensen *et al.,* 1983) and the amber14sb force field was implemented (Lee *et al.,* 2020). System was neutralized with K^+ and Cl^- ions that were placed using the Monte-Carlo method. Neutralization was followed by addition of KCl to reach a concentration of 0.15 mol/l (150 mM), temperature was set to 310 K at a neutral pH. The CHARMM-GUI Solution Builder was also used for the introduction of the I80T mutation on the G_{β} chain (Jo *et al*., 2008).

For the simulations of GIRK2 bound to $G_{\beta\gamma}$, PIP_2 and Na^+ embedded in a POPC bilayer in the presence of 10 R- or S- ethosuximide (ETX) molecules and an applied electric field of +10 or -10 mV, the simulation box was prepared using standard GROMACS modules (version 2021.5) (Abraham *et al.,* 2015; www2) together with the amber99sb force field (Hornak *et al.,* 2006). PIP_2 parameters were obtained as described by my colleagues in their previous work (Lee *et al.,* 2016). ETX parameters were generated using SwissParam (Zoete *et al.,* 2011). The channel was placed in a lipid membrane using the inflate method (Kandt *et al.,* 2007) with Berger lipid parameters (Berger *et al.,* 1997).

3.3 Simulations

To perform wt and I80T MD simulations, GROMACS software (version 2021.5) (Abraham *et al.,* 2015; www2) was used. Input files for minimization, equilibration and production were provided by CHARMM-GUI (Jo *et al*., 2008).

For all setups, respective to equilibration and production, time step for all simulations was set to 2 fs, the leap-frog integrator was implemented to solve the equations of motion and the LINCS algorithm was used to constrain protein bonds (Hess *et al*., 1997). The particle mesh Ewald method was used for calculations of long-range electrostatic interactions at each step while short-range electrostatic interactions and van der Waals cutoff of 1 nm was used (Darden *et al*., 1993).

3.3.1 Energy minimization

To ensure an appropriate, stabilized geometry and avoid steric clashes, the structure was relaxed through the steepest descent energy minimization, where the Verlet algorithm was used and protein atoms were restrained with a force constant of 1 000 kJ/mol/nm to their starting positions. The long-range electrostatic interactions were treated with cutoff, for short-range electrostatic interactions and van der Waals cutoff of 1.2 nm was used.

3.3.2 NVT equilibration

To equilibrate the ions and solvent around the protein, equilibration steps were implemented. The NVT (constant number of particles, volume and temperature) equilibration run was performed for 1 ns. Temperature was coupled via the V-rescale thermostat to 310 K (Bussi *et al*., 2007) and a coupling constant of 0.1 ps. Initial velocities were assigned and selected from the Maxwell-Boltzmann distribution at 310 K.

3.3.3 NPT equilibration

The NPT (constant number of particles, pressure and temperature) equilibration run was performed for 5 ns. Temperature was coupled via the Nose-Hoover thermostat to 310 K (Evans & Holian, 1985) and a coupling constant of 0.5 ps. For pressure coupling, the C-rescale barostat was used with a 1 bar reference pressure with isotropic scaling and a constant of 5 ps.

3.3.4 Production run

A 500 ns free MD simulation run was performed 3 times for each, the wt and I80T $G_{\beta\gamma}$ subunit. For the simulations of GIRK2 bound $G_{\beta\gamma}$, an electric field of +/-10mV/nm was applied. Temperature was coupled via the Nose-Hoover thermostat to 310 K (Evans & Holian, 1985) and a coupling constant of 0.5 ps. For pressure coupling, the Parrinello-Rahman barostat was used with a 1 bar reference pressure with isotropic scaling (Parrinello & Rahman, 1981) and a constant of 5 ps.

3.4 Analysis

Upon production runs completion, the GROMACS trjconv module (Abraham *et al.,* 2015; www2) was used to process the trajectory to account for periodicity in the system. The structure was centered by the G_{β} chain in order for all atoms to remain within the box. Protein was then visualized using VMD (Humphrey *et al.,* 1996) and PyMOL (Schrödinger, 2010). LigandScout (Wolber & Langer, 2005) was used for the visualization of isoleucine and threonine. For the GIRK2 bound $G_{\beta\gamma}$, the $G_{\beta\gamma}$ subunits were extracted from the simulations for analysis.

3.4.1 Evaluation of thermodynamic properties

The GROMACS energy module (Abraham *et al.,* 2015; www2) was used to extract thermodynamic properties (potential energy, temperature, pressure, density) from the system preparation and simulations for analysis. For visualization of data, the XMGRACE plotting tool (version 5.1.25) (Turner, 2005) was used.

3.4.2 Evaluation of trajectory and structural changes

The GROMACS modules hbond, sasa, gyrate, rms, and rmsf (Abraham *et al.,* 2015; www2) were used to analyze hydrogen bonds and calculate the solvent accessible surface area (SASA), radius of gyration, root mean square deviation (RMSD), and root mean square fluctuation (RMSF), respectively, to analyze trajectory and structural changes of $G_{\beta\gamma}$. To visualize the data, XMGRACE plotting tool (version 5.1.25) (Turner, 2005) was used. A python script was created to obtain average values for hydrogen bond analysis, SASA, radius of gyration, and RMSD. Hydrogen bond occupancy analysis was calculated in VMD (Humphrey *et al.,* 1996). The figures displaying average RMSF values were plotted in Microsoft Excel for Mac Version 16.73 (2023).

4 Results

In order to investigate the structural effect of pathological variant I80T on $G_{\beta\gamma}$, we conducted MD simulations with wt and I80T $G_{\beta\gamma}$ complex unbound in water. To compare the dynamics of unbound wt $G_{\beta\gamma}$ to GIRK2-bound $G_{\beta\gamma}$, we analyzed MD simulations of GIRK2 bound to $G_{\beta\gamma}$, PIP_2 and Na^+ embedded in a lipid bilayer in the presence of 10 R- or S- ETX molecules and an electric field of +10 or -10 mV was applied (PDB: 4KFM); these simulations were provided by my colleague Theres Friesacher, BSc MSc. An overview of structures and conditions used for analyzed MD simulations is provided in Table 3. In this work, data will be further referred to as stated in the first and last column.

Table 3 – Summary of structures used in MD simulations for analysis. For increased clarification, the table shows a number of MD runs performed (in the case of ETX structures, the number of $G_{\beta\gamma}$ subunits per 1 MD run), length of single MD runs along with a description of the structures and how they are further referred to as in this work.

Structure	# of MD runs	# of Gβγ subunits	MD length	MD description	Structure description	Additional remarks	Referred to as
wt Gβγ	3	1	500 ns	**unbound Gβγ** in solution	structure of Gβγ subunit extracted from 4KFM and modeled in solution	N/A	wt Gβγ
I80T Gβγ	3	1					I80T Gβγ
ETR+10mV	1	4	500 ns	**GIRK2 bound Gβγ;** GIRK2 bound to Gβγ, PIP2 and Na+ in presence of 10 ETX molecules in membrane	structure of Gβγ subunit extracted from 4KFM and modeled in membrane	in presence of 10 R-ETX molecules with applied electric field of +/-10mV/nm	ETR+10mV
ETR-10mV	1	4					ETR-10mV
ETS+10mV	1	4				in presence of 10 S-ETX molecules with applied electric field of +/-10mV/nm	ETS+10mV
ETS-10mV	1	4					ETS-10mV

4.1 Evaluation of thermodynamic properties

Prior to conducting free runs of unbound $G_{\beta\gamma}$ MD simulations, we ensured the system has appropriate geometry and the structure is relaxed through the processes of energy minimization and equilibration. Plots of thermodynamic properties demonstrating proper equilibration of the system are shown in Figure S1 (Supplementary).

4.2 Evaluation of trajectory and structural changes

The I80T mutation results in the presence of additional hydrogen bonds between the side chain of Thr80 and surrounding residues from the $G_{\beta\gamma}$ dimer compared to wt protein.

However, we do not see an effect of these interactions on stability, conformation and dynamics of $G_{\beta\gamma}$. Figure 7 presents the aligned structures of unbound wt and I80T $G_{\beta\gamma}$, and GIRK2-bound $G_{\beta\gamma}$ at 500 ns. No major difference between the structures could be observed. For increased clarity and comparability, data in the Results section is described by the means of average values, and the un-averaged data for all parameters and specific MD runs is summarized in Table S1 (Supplementary).

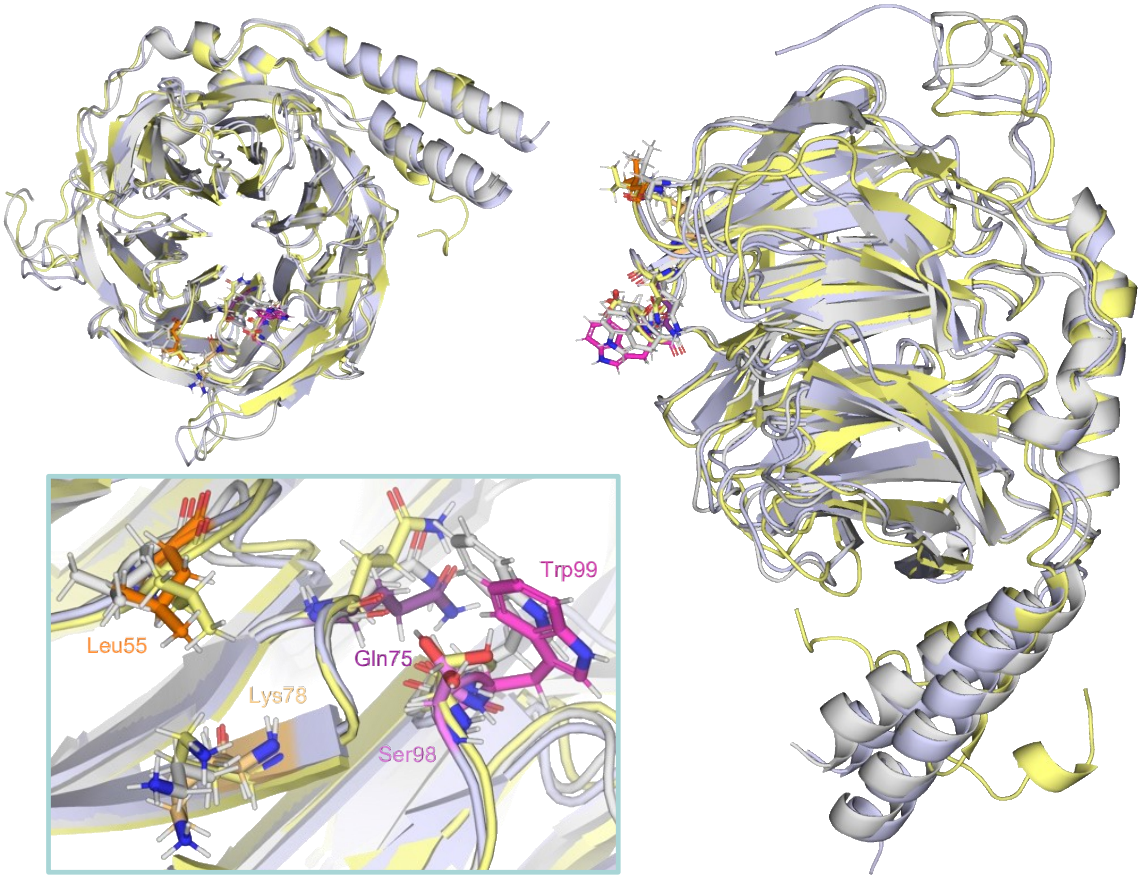

Figure 7 – Aligned structures of $G_{\beta\gamma}$ from conducted MD simulations (PDB: 4KFM). Wt $G_{\beta\gamma}$ is shown in grey, I80T $G_{\beta\gamma}$ is show in purple, and GIRK2-bound ETS +10 mV $G_{\beta\gamma}$ is shown in yellow. Residues located at the GIRK2-$G_{\beta\gamma}$ binding interface are highlighted. Snapshots represent the simulation end states at 500 ns.

4.2.1 Hydrogen bond analysis

Since hydrogen bonds stabilize secondary structures of proteins and protein-ligand complexes, hydrogen bond analysis in terms of their number or duration plays a key role in evaluating MD simulations. We found that the side chain of Thr80 in the I80T $G_{\beta\gamma}$ can form additional hydrogen bonds compared to wt $G_{\beta\gamma}$. The average number of hydrogen bonds formed between the Thr80 side chain of I80T G_{β} and its surrounding residues is below 1 for all of the runs, indicating a low occurrence of this interaction (Table 4).

Table 4 – Average number of hydrogen bonds formed between the side chain of Thr80 and surrounding residues in I80T $G_{\beta\gamma}$. The table displays averages of data from all timeframes of 3 MD runs, each with a length of 500 ns.

Average number of side chain Thr80 hbonds per timeframe	
	I80T Gβγ
MD run 1	0.810
MD run 2	0.611
MD run 3	0.361

Hydrogen bonds that hold the β sheet together are not influenced by the I80T pathogenic variant. A closer analysis of hydrogen bond occupancy performed in VMD (Table 5) revealed that 3 interactions between the backbone of Ile80/Thr80 and backbone or side chain of Ser72 (bond #1, #2, #3 for wt and #1, #2 and #8 for I80T) are equally present among the wt and I80T $G_{\beta\gamma}$, indicating no influence of the mutation on the conformation of β sheet (Figure 8).

Table 5 – Occupancy of hydrogen bonds formed between Ile80/Thr80 and selected residues in wt/I80T $G_{\beta\gamma}$ in solution. Hydrogen bonds are numbered based on highest average occupancy. Hydrogen bonds highlighted in blue hold the β sheet together and are not influenced by the I80T mutation. Residue Lys78 that is localized in the $G_{\beta\gamma}$-GIRK2 binding interface is highlighted in bold.

Donor	Acceptor	Bond #	Occupancy			
			MD run 1	MD run 2	MD run 3	Average
wt Gβγ						
Ile80-backbone	Ser72-backbone	1	47.48%	50.44%	49.64%	**49.19%**
Ser72-backbone	Ile80-backbone	2	25.66%	24.26%	28.54%	**26.15%**
Ser72-sidechain	Ile80-backbone	3	0.08%	0%	0.12%	**0.07%**
					Summary	**75.41%**
I80T Gβγ						
Thr80-backbone	Ser72-backbone	1	41.45%	32.77%	52.88%	**42.37%**
Ser72-backbone	Thr80-backbone	2	27.26%	32.29%	22.10%	**27.22%**
Thr80-sidechain	His54-sidechain	3	22.94%	4.32%	7.11%	**11.46%**
Thr80-sidechain	Leu79-backbone	4	2.36%	3.44%	3.56%	**3.12%**
Thr80-sidechain	**Lys78-backbone**	5	1.20%	4.28%	0.08%	**1.85%**
Trp82-sidechain	Thr80-sidechain	6	0%	0.36%	0.88%	**0.41%**
Thr80-sidechain	Ser72-backbone	7	0%	0%	0.40%	**0.13%**
Ser72-sidechain	Thr80-backbone	8	0.04%	0.12%	0.12%	**0.09%**
Lys78-sidechain	Thr80-sidechain	9	0%	0.12%	0.04%	**0.05%**
Lys89-sidechain	Thr80-sidechain	10	0%	0%	0.12%	**0.04%**
Thr80-sidechain	Gly53-backbone	11	0.04%	0%	0%	**0.01%**
					Summary	**86.75%**

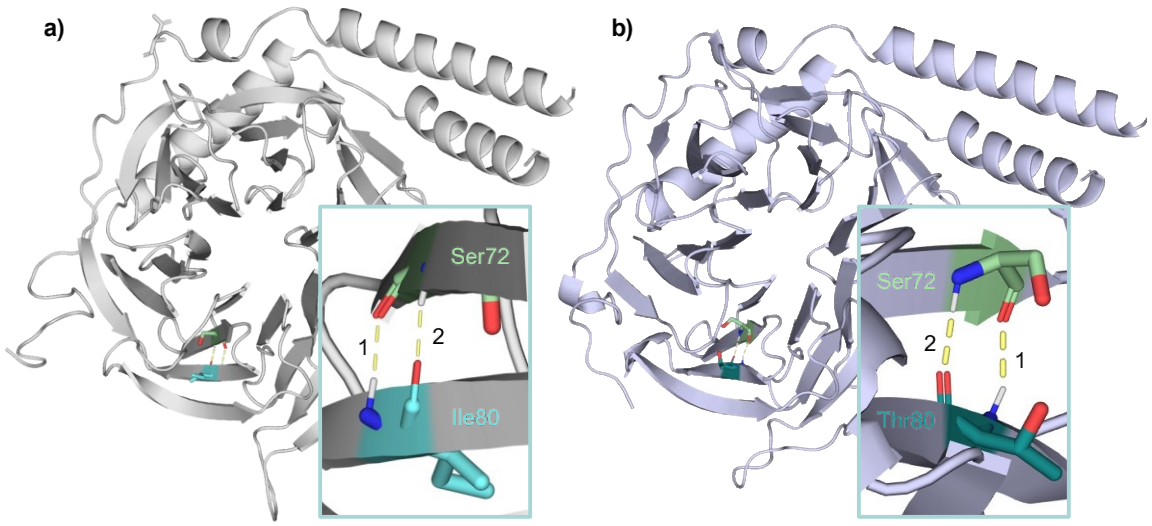

Figure 8 – Hydrogen bonds between Ser72 and Ile80/Thr80 (PDB: 4KFM). These interactions hold the β sheet together and are not influenced by the I80T pathogenic mutation. **a) wt $G_{\beta\gamma}$** is represented in grey and **b) I80T $G_{\beta\gamma}$** is shown in purple. For reference regarding bond numbering, see Table 5 above.

Table 5 demonstrates that the side chain of Thr80 in the I80T mutant can make 8 additional interactions with surrounding residues of G_β compared to the wt bearing Ile80. This is because the hydroxy group of threonine side chain can act as both, hydrogen bond donor and acceptor (Figure 6). Occurrence of these interactions ranges from 0.01% to 11.46% among 3 MD runs. The residues of G_β interacting with Thr80 are highlighted in Figure 9a, along with the more occurring hydrogen bonds shown as well. Apart from the interaction with Ser72, the most common interaction was between Thr80 side chain and His54 side chain (bond #3) with an occupancy of 11.46% (Figure 9b) followed by bond #4 with an occupancy of 3.12% between Thr80 side chain and backbone of Leu79 (Figure 9c). As Lys78 is located in the $G_{\beta\gamma}$-GIRK2 binding interface, bond #5 and #9, despite their low occupancy, could be of relevance (Figure 9c and d).

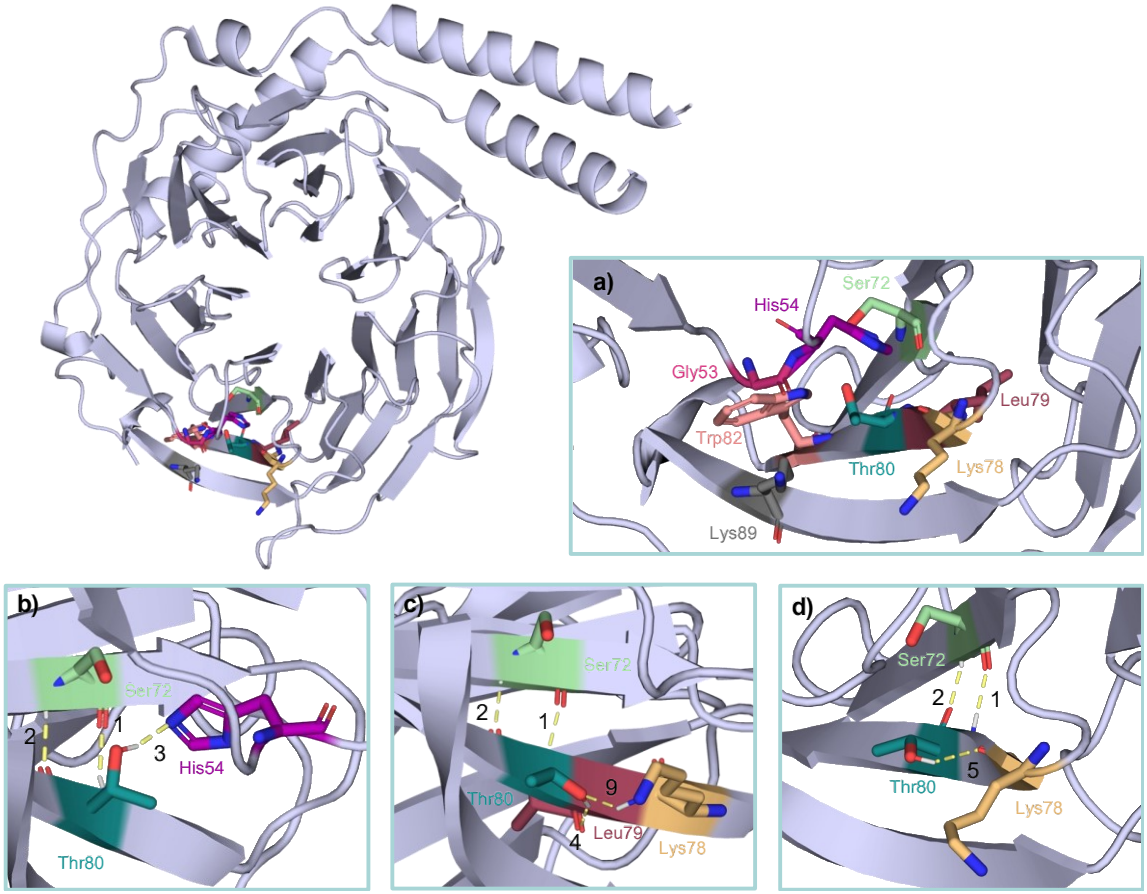

Figure 9 – Selected hydrogen bond interactions between Thr80 and surrounding residues in the I80T pathological variant (PDB: 4KFM). I80T $G_{\beta\gamma}$ is represented in purple. Bonds #1 and #2 between Thr80 (teal) and Ser72 (green) hold the β sheet together. **a)** All I80T G_{β} residues that Thr80 interacts with are highlighted. Among these, Lys78 (yellow) is also a part of the GIRK2-$G_{\beta\gamma}$ binding interface. **b)** Interaction #3 between donor Thr80 side chain (teal) and acceptor His54 side chain (magenta). **c)** Interaction #4 between donor Thr80 side chain (teal) and acceptor Leu79 backbone (raspberry). In interaction #9, Thr80 side chain (teal) acts as an acceptor, the donor is side chain Lys78 (yellow) located at the GIRK2-$G_{\beta\gamma}$ binding interface. **d)** Interaction #5 between donor Thr80 side chain (teal) and acceptor Lys78 backbone (yellow) located at the GIRK2-$G_{\beta\gamma}$ binding interface.

Stability of $G_{\beta\gamma}$ dimer formation can be evaluated by analyzing the formation of hydrogen bonds between G_{β} and G_{γ}. Shown in Figure 10, hydrogen bond formation between G_{β} and G_{γ} stably fluctuates in the range of 10 to 30 bonds throughout the 500 ns course of MD simulations for unbound wt and I80T $G_{\beta\gamma}$ and GIRK2-bound wt $G_{\beta\gamma}$.

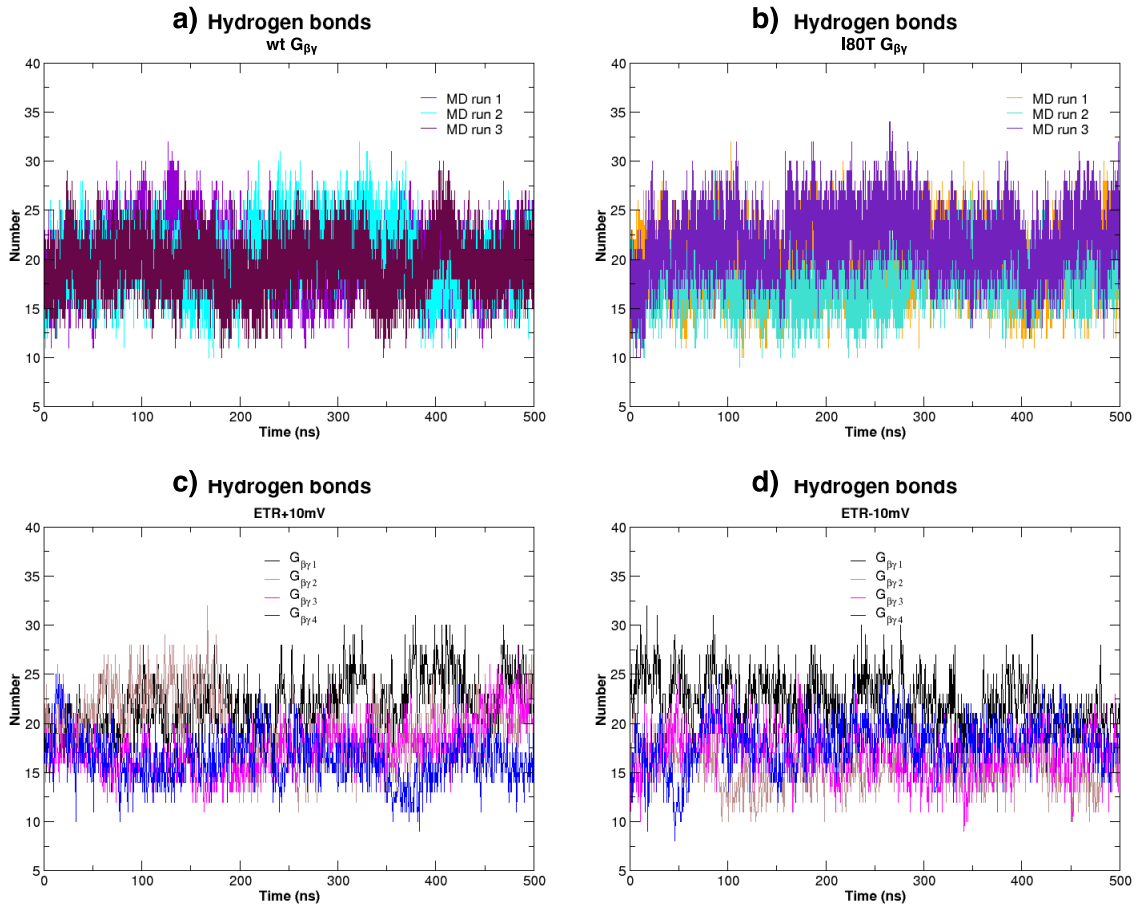

Figure 10 – Number of hydrogen bonds formed between G_β and G_γ throughout simulations. Hydrogen bonds for pairs within 0.35 nm are displayed. Hydrogen bonds between G_β and G_γ of unbound dimer for 3 MD runs, each 500 ns long, are shown in **a)** wt $G_{\beta\gamma}$ and **b)** I80T $G_{\beta\gamma}$. Data for GIRK2-bound $G_{\beta\gamma}$ is shown in **c)** and **d)** where data from ETR simulations is represented as an example, as the data for ETS simulations follows the same trend. Data from ETS simulations is shown in Figure S2 (Supplementary).

The average number of hydrogen bonds between G_β and G_γ monomers was calculated, ranging from 18.19 to 19.80 in all of the simulated structures (Table 6). Our data indicates that dimer formation is equally stable for the wt, I80T mutated, unbound and GIRK2-bound $G_{\beta\gamma}$.

Table 6 – Average number of hydrogen bonds formed between G_β and G_γ per timeframe. The table displays averages of data from all timeframes of 3 MD runs unbound $G_{\beta\gamma}$ (shown in pink) and 4 GIRK2-bound $G_{\beta\gamma}$ subunits (shown in grey). Full, un-averaged data is shown in Table S1.

	wt Gβγ	I80T Gβγ	ETR+10mV	ETR-10mV	ETS+10mV	ETS-10mV
Hydrogen bonds average **(#)**	**19.78**	**19.80**	**18.84**	**18.19**	**19.40**	**19.14**

4.2.2 SASA analysis

SASA is a measure of the protein surface area that is accessible to molecules of solvent. It is an essential decisive factor to assess protein folding and stability, and therefore key for evaluation of structural differences in MD simulations. We found that SASA for wt $G_{\beta\gamma}$, I80T $G_{\beta\gamma}$ and ETX $G_{\beta\gamma}$ does not differ in nature. Throughout the course of simulations for all $G_{\beta\gamma}$ structures, SASA fluctuates between 170 and 190 nm in comparable trends (Figure 11).

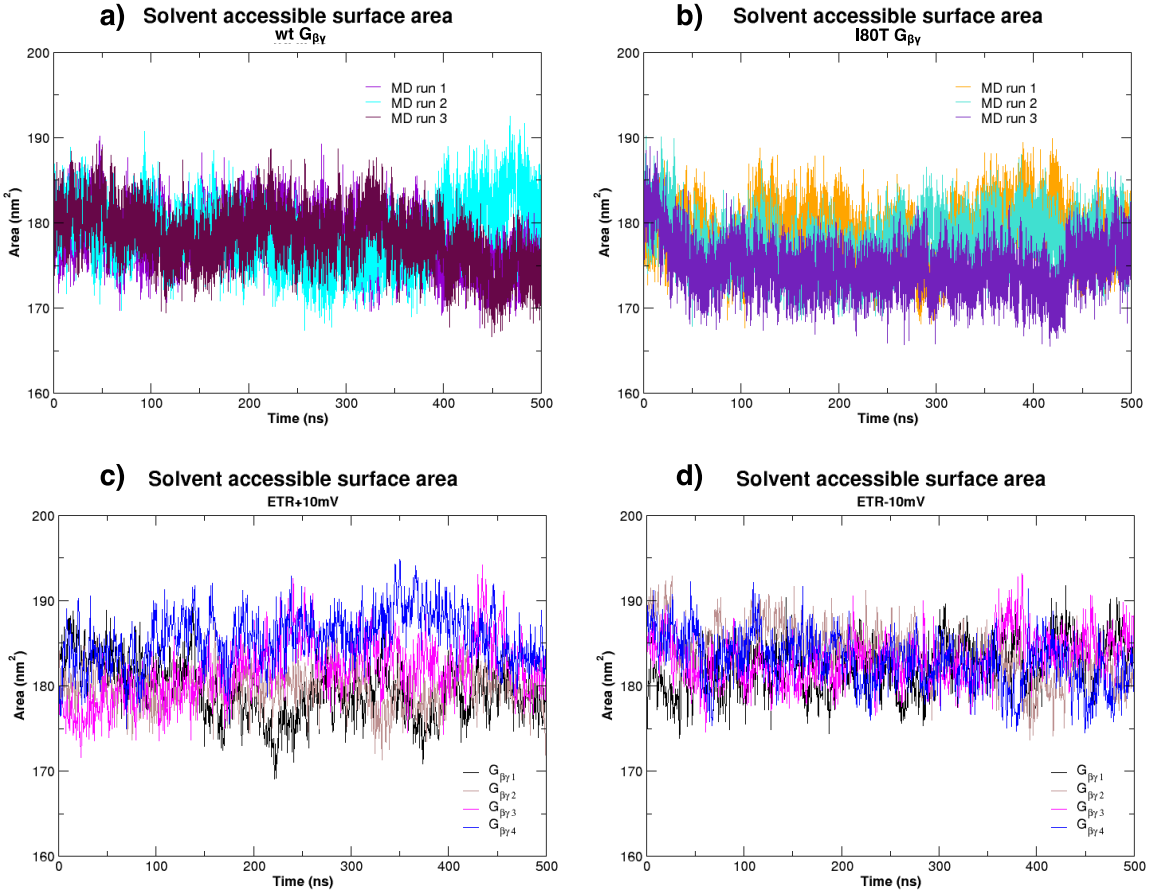

Figure 11 – Solvent accessible surface area of $G_{\beta\gamma}$ throughout simulations. SASA in nm^2 of unbound $G_{\beta\gamma}$ is shown for **a)** wt $G_{\beta\gamma}$ and **b)** I80T $G_{\beta\gamma}$. Data for GIRK2-bound $G_{\beta\gamma}$ is represented in **c)** and **d)** where data from ETR simulations is shown as an example, as the data for ETS simulations follows the same trend. Data from ETS simulations is shown in Figure S3 (Supplementary).

As SASA fluctuations in all simulations are stable, average values were also calculated and are in the range of 177.10 to 184.11 nm^2, with only a small difference in values observed, indicating no effect of the I80T mutation on folding and stability of $G_{\beta\gamma}$ (Table 7).

Table 7 – Average SASA (in nm²) of $G_{\beta\gamma}$ per timeframe. The table displays averages of data from all timeframes of 3 MD runs unbound $G_{\beta\gamma}$ (shown in pink) and 4 GIRK2-bound $G_{\beta\gamma}$ subunits (shown in grey). Full, un-averaged data is shown in Table S1.

	wt Gβγ	I80T Gβγ	ETR+10mV	ETR-10mV	ETS+10mV	ETS-10mV
SASA average (nm2)	**178.43**	**177.10**	**181.59**	**182.99**	**181.26**	**184.11**

4.2.3 Radius of gyration analysis

Radius of gyration measures compactness of a simulated protein. We found that $G_{\beta\gamma}$ radius of gyration maintains relatively steady values around 2.15 to 2.20 nm for all simulated $G_{\beta\gamma}$ structures, indicating the protein is compact and stably folded in all simulations. As no considerable change in radius of gyration is observed, $G_{\beta\gamma}$ does not unfold during our 500 ns long MD simulations and there are no differences among wt and mutated variants (Figure 12).

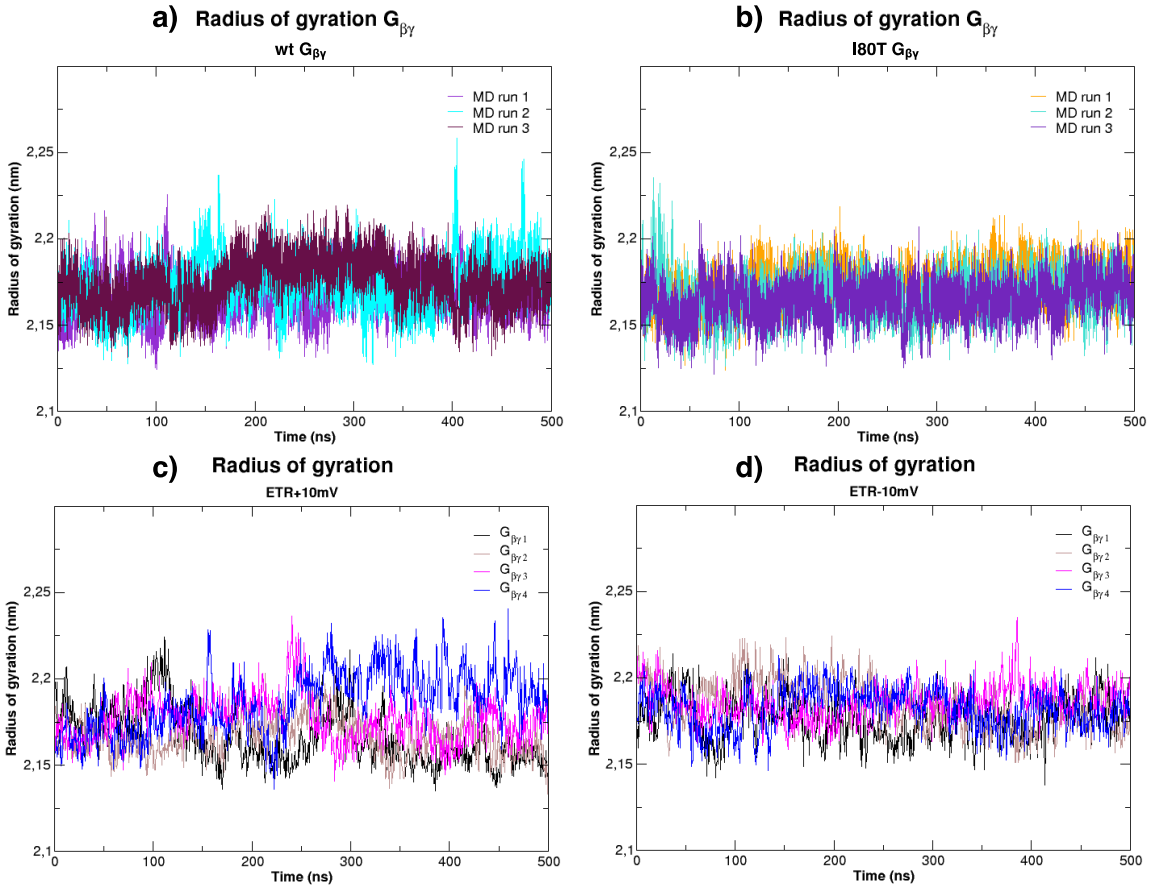

Figure 12 – Radius of gyration for $G_{\beta\gamma}$ throughout simulations. Radius of gyration in nm of unbound $G_{\beta\gamma}$ is shown for **a)** wt $G_{\beta\gamma}$ and **b)** I80T $G_{\beta\gamma}$. Data for GIRK2-bound $G_{\beta\gamma}$ is represented in **c)** and **d)** where data from ETR simulations is shown as an example, as the data for ETS simulations follows the same trend. Data from ETS simulations is shown in Figure S4 (Supplementary).

Average values for $G_{\beta\gamma}$ radius of gyration in all MD simulations were also calculated to demonstrate data comparability. Radius of gyration on average ranges from 2.166 to 2.182 nm, indicating no difference between unbound, bound, wt and I80T $G_{\beta\gamma}$ (Table 8).

Table 8 – Average radius of gyration (in nm) of $G_{\beta\gamma}$ per timeframe. The table displays averages of data from all timeframes of 3 MD runs unbound $G_{\beta\gamma}$ (shown in pink) and 4 GIRK2-bound $G_{\beta\gamma}$ subunits (shown in grey). Full, un-averaged data is shown in Table S1.

	wt Gβγ	I80T Gβγ	ETR+10mV	ETR-10mV	ETS+10mV	ETS-10mV
Radius of gyration average **(nm)**	**2.172**	**2.168**	**2.174**	**2.182**	**2.166**	**2.179**

4.2.4 RMSD analysis

RMSD is a measure of how much does the structure of simulated protein deviate from a reference geometry over the course of MD simulation. It is an essential analysis feature to compare how much the system changes or evolves compared to the starting structure. We calculated RMSD for both, protein backbone and full protein (backbone and side chains), compared to the minimized equilibrated structure, and found RMSD does not differ between wt $G_{\beta\gamma}$, I80T $G_{\beta\gamma}$ and ETX $G_{\beta\gamma}$. Throughout simulations, RMSD followed a steady trend fluctuating between 0.1 to 0.35 nm (protein backbone) or between 0.15 to 0.4 nm (full protein) with no important spikes presenting on the plots, indicating the structure is stable and no major conformational changes were present. Plots for RMSD backbone are shown in Figure 13 and plots for RMSD protein are included in Figure S6 (Supplementary) due to high data comparability.

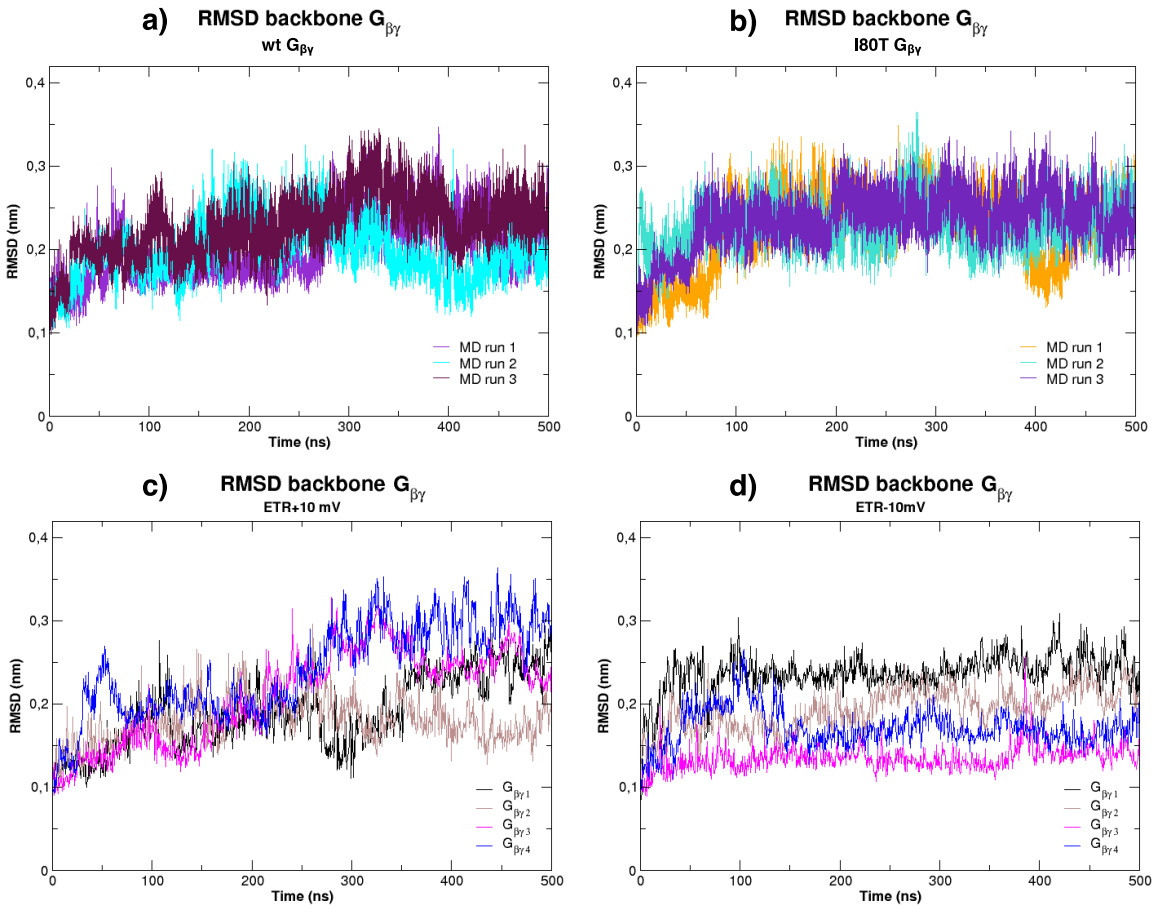

Figure 13 – RMSD of $G_{\beta\gamma}$ backbone after 1sq fit to backbone throughout simulations. RMSD in nm is shown relative to the structure of the minimized, equilibrated system. RMSD of unbound $G_{\beta\gamma}$ is shown for **a)** wt $G_{\beta\gamma}$ and **b)** I80T $G_{\beta\gamma}$. Data for GIRK2-bound $G_{\beta\gamma}$ is represented in **c)** and **d)** where data from ETR simulations is shown as an example, as the data for ETS simulations follows the same trend. Data from ETS simulations is shown in Figure S5 (Supplementary).

Average values of RMSD were calculated to range from 0.184 to 0.229 nm for backbone RMSD and 0.245 to 0.296 nm for full protein RMSD (backbone + side chain). Higher RMSD values for full protein were expected, as greater movement of residue side chains is natural. Even though the highest RMSD values for both backbone and full protein are observed in the I80T mutant, the difference compared to wt $G_{\beta\gamma}$ is subtle, indicating all simulated structures deviate from the reference geometry (minimized equilibrated system) to the same and limited extent (Table 9).

Table 9 – Average RMSD values (in nm) of $G_{\beta\gamma}$ per timeframe. The table displays averages of data from all timeframes of 3 MD runs unbound $G_{\beta\gamma}$ (shown in pink) and 4 GIRK2-bound $G_{\beta\gamma}$ subunits (shown in grey). Full, un-averaged data is shown in Table S1.

	wt Gβγ	I80T Gβγ	ETR+10mV	ETR-10mV	ETS+10mV	ETS-10mV
RMSD backbone average (nm)	**0.208**	**0.229**	**0.205**	**0.184**	**0.186**	**0.188**
RMSD protein average (nm)	**0.272**	**0.296**	**0.264**	**0.245**	**0.248**	**0.250**

4.2.5 RMSF analysis

RMSF measures the fluctuation of atoms or residues during the simulation to identify the most mobile regions of the structure. It is a key parameter to identify residues that are flexible even after the structure has stabilized. We calculated RMSF for G_{β} and G_{γ} separately compared to the minimized, equilibrated structures and found no relevant differences in RMSF values of important residues.

4.2.5.1 G_{β} RMSF analysis

We found that G_{β} RMSF values for Thr80 in the I80T $G_{\beta\gamma}$ mutant do not differ compared to Ile80 in the wt $G_{\beta\gamma}$ variant. The average RMSF protein value for wt Ile80 was 0.076 nm and 0.082 nm for I80T Thr80. The side chain RMSF was calculated 0.089 nm for wt and 0.099 for I80T $G_{\beta\gamma}$, indicating the residue 80 is fixed in both variants and the mutation has no effect on structural dynamics (Table 10).

Table 10 – RMSF values for Ile80 and Thr80 in the wt and I80T $G_{\beta\gamma}$ variants. RMSF values are shown for full protein (backbone+side chain) and for side chain only. Each MD run was 500 ns long.

	RMSF protein (nm)	RMSF side chain (nm)
	wt - Ile80	
MD run 1	0.0743	0.0855
MD run 2	0.0732	0.0862
MD run 3	0.0805	0.0947
average	**0.076**	**0.089**
	I80T - Thr80	
MD run 1	0.0765	0.0883
MD run 2	0.0838	0.1013
MD run 3	0.0861	0.1076
average	**0.082**	**0.099**

G_{β} RMSF values do not differ between wt $G_{\beta\gamma}$, I80T $G_{\beta\gamma}$ and ETX $G_{\beta\gamma}$ structures. In all simulations for majority of the residues, RMSF steadily fluctuated around the 0.1 to 0.2 nm range, not deviating much from their average position. A few spikes reaching to ~ 0.6 nm observed in Figure 14 and Figures S7 and S9 (Supplementary) indicate higher divergence and mobility of some residues from their average position, however, the trend is the same for all structures, indicating no I80T related influence. These residues are also not located in the GIRK2-$G_{\beta\gamma}$ binding interface, nor interact with Thr80.

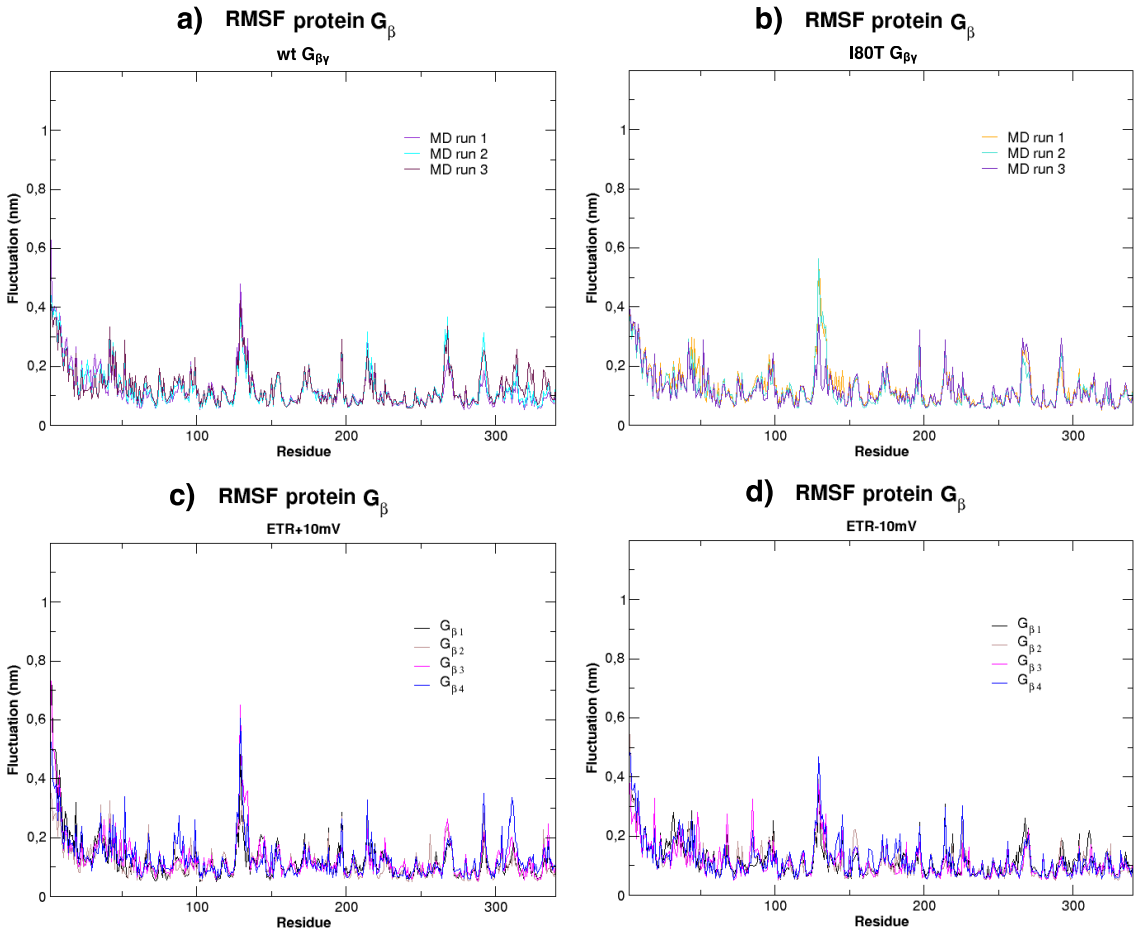

Figure 14 – RMSF of G_β protein throughout simulations. RMSF in nm is shown relative to the structure of the minimized, equilibrated system as the square root of variance of fluctuation around the average position. RMSF of unbound G_β is shown for **a)** wt $G_{\beta\gamma}$ and **b)** I80T $G_{\beta\gamma}$. Data for GIRK2-bound G_β is represented in **c)** and **d)** where data from ETR simulations is shown as an example, as the data for ETS simulations follows the same trend. Data from ETS simulations is shown in Figure S7 (Supplementary).

Average RMSF values were calculated for selected residues located either in the GIRK2-$G_{\beta\gamma}$ binding interface, or forming hydrogen bonds with Thr80 in the I80T mutant. Highest RMSF values were calculated for Trp99 reaching 0.272 nm supporting that these residues are rather rigid during simulations. Similarly, no greater RMSF differences are observed between the wt, I80T and ETX structures indicating no influence of the I80T mutation on $G_{\beta\gamma}$ dynamics (Table 11).

Table 11 – Average RMSF values for selected residues of wt, I80T and ETX $G_{\beta\gamma}$. The data displays average values for 3 MD runs for unbound $G_{\beta\gamma}$ and for 4 $G_{\beta\gamma}$ subunits per 1 MD run of GIRK2-bound $G_{\beta\gamma}$, all simulations were 500 ns long. Residues from GIRK2-$G_{\beta\gamma}$ binding interface and forming hydrogen bonds with Thr80 in GIRK2-$G_{\beta\gamma}$ were selected. RMSF values are shown for full protein (backbone+side chain) for all structures and for $G_{\beta\gamma}$ in solution, RMSF side chain is also shown. Color code of residues is respective to structural figures.

	RMSF side chain (nm)		RMSF protein (nm)					
	wt Gβγ	I80T Gβγ	wt Gβγ	I80T Gβγ	ETR+10mV	ETR-10mV	ETS+10mV	ETS-10mV
residues in the GIRK2-Gβγ binding interface								
Leu55	0.202	0.217	0.164	0.176	0.142	0.137	0.141	0.125
Gln75	0.221	0.210	0.179	0.174	0.137	0.140	0.157	0.147
Lys78	0.192	0.207	0.154	0.168	0.120	0.126	0.113	0.140
Ser98	0.153	0.219	0.127	0.175	0.102	0.126	0.116	0.148
Trp99	0.253	0.272	0.220	0.237	0.183	0.196	0.174	0.217
residues forming hydrogen bonds with Thr80 in I80T Gβγ								
Gly53	0.105	0.109	0.093	0.100	0.106	0.086	0.114	0.092
His54	0.081	0.106	0.084	0.103	0.106	0.097	0.144	0.095
Ser72	0.087	0.085	0.067	0.069	0.069	0.064	0.066	0.068
Lys78	0.192	0.207	0.154	0.168	0.120	0.126	0.113	0.140
Leu79	0.102	0.114	0.086	0.097	0.086	0.089	0.093	0.097
Trp82	0.096	0.096	0.091	0.089	0.074	0.089	0.074	0.131
Lys89	0.183	0.185	0.156	0.158	0.133	0.144	0.125	0.128

4.2.5.2 G_{γ} RMSF analysis

While there was no difference in the RMSF trend between the unbound wt and I80T $G_{\beta\gamma}$ structures, we found differences in G_{γ} RMSF values between the unbound $G_{\beta\gamma}$ and GIRK2-bound $G_{\beta\gamma}$ structures. Shown in Figure 15 and Figures S8 and S9 (Supplementary), RMSF for residues ~ 15 to 60 steadily fluctuated around the 0.1 to 0.3 nm range in all simulations, residues not deviating from their average position, as no spikes that would indicate higher residue mobility are observed. However, G_{γ} N-terminal residues of the GIRK2-bound ETX structures fluctuate considerably more compared to residues of unbound $G_{\beta\gamma}$ structures, reaching ~ 0.7 nm compared to ~ 0.25 nm. Opposingly, G_{γ} C-terminal residues showed more fluctuations in the unbound $G_{\beta\gamma}$ structures reaching ~ 0.7 nm, compared to ~ 0.5 nm observed in GIRK2-bound ETX structures. This indicates that while there is no observed effect of the I80T mutation on RMSD, binding of $G_{\beta\gamma}$ to GIRK2 could evoke additional allosteric changes in the G_{γ} subunit, GIRK2 channel or both.

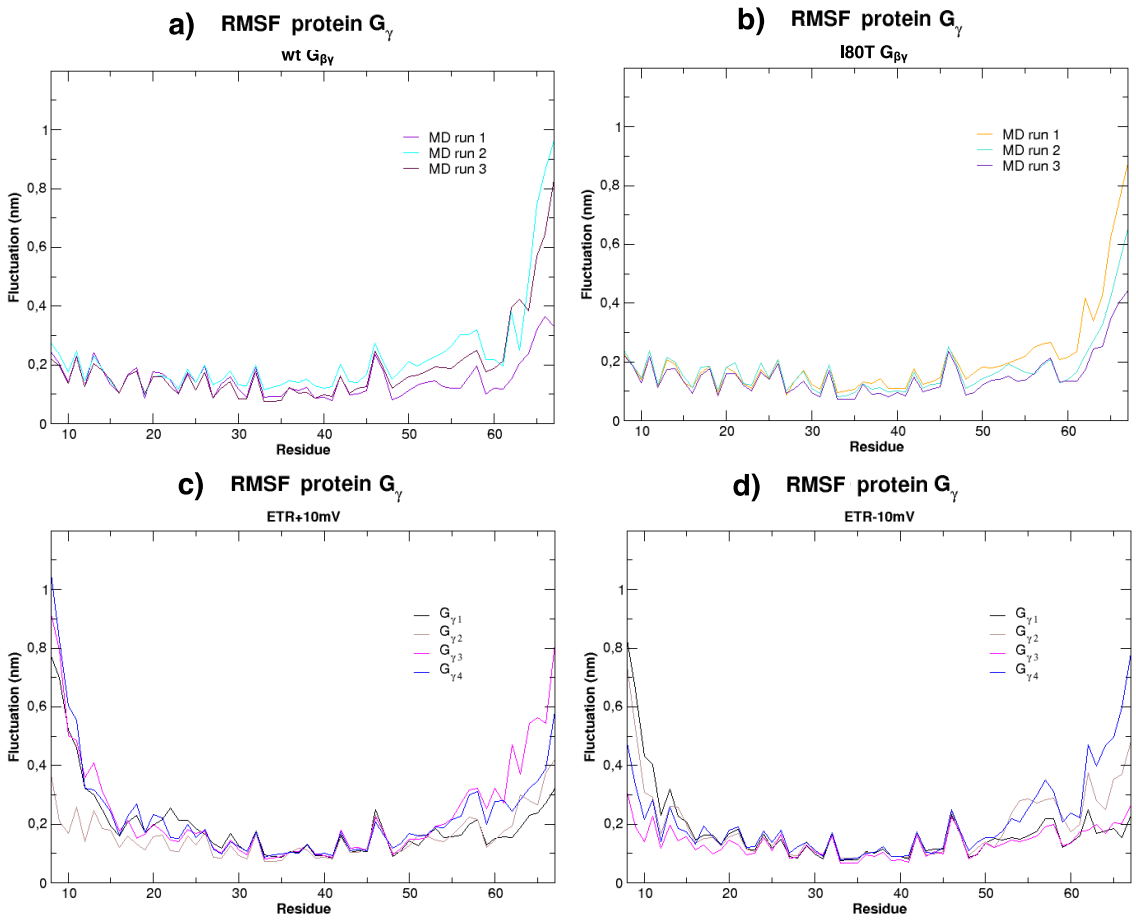

Figure 15 – RMSF of G_γ protein throughout simulations. RMSF in nm is shown relative to the structure of the minimized, equilibrated system as the square root of variance of fluctuation around the average position. RMSF of unbound G_γ is shown for **a)** wt $G_{\beta\gamma}$ and **b)** I80T $G_{\beta\gamma}$. Data for GIRK2-bound G_γ is represented in **c)** and **d)** where data from ETR simulations is shown as an example, as the data for ETS simulations follows the same trend. Data from ETS simulations is shown in Figure S8 (Supplementary).

5 Discussion

GNB1 encephalopathy is a genetically determined neurodevelopmental syndrome, where the LoF I80T pathological variant is the most abundant among patients (Revah-Politi *et al.,* 2020). As the *GNB1* gene is highly intolerant to genetic variation, disruptions in protein structure caused by mutations can result in profound changes in its function (Da Silva *et al.,* 2021; Petrovski *et al.,* 2016). However, information on the functional changes at the molecular level caused by *GNB1* pathogenic variants has been limited so far. The I80T mutation-induced changes in $G_{\beta\gamma}$ were first studied by Reddy et al. in 2021 who suggest a strong LoF effect towards GIRK2 homomeric assemblies (Reddy *et al.,* 2021). Our study investigated structural changes of the $G_{\beta\gamma}$ subunit caused by the mutation I80T, as allosteric changes could prevent further downstream GIRK2 activation.

It was hypothesized that a potential link between the I80T variant pathology could be on the level of $G_{\beta\gamma}$ dimer formation, as GNB1 encephalopathy-causing LoF variants G64V and A106T have previously been shown to influence the stability of $G_{\beta\gamma}$ dimer (Lohmann *et al.,* 2017). Our data indicates that the wt and I80T $G_{\beta\gamma}$ dimer formation is stable (Figure 10), and that the effect of the mutation on the stability of the dimer in solution is limited on the 500 ns time scale that was simulated. These findings are supported by experimental data where the formation of $G_{\beta\gamma}$ dimers was assessed using bimolecular fluorescence complementation in HEK cells. Not only the I80T G_{β} mutant, but also K78R and I80N variants were shown to form dimers with G_{γ} similarly to the wt protein. Additionally, GPCR-induced activation of G protein trimers was assessed using a BRET $G_{\beta\gamma}$ release assay, where all three mutants showed a dopamine-induced response similar to wt protein, suggesting there is no significant effect of these mutations on the $G_{\alpha\beta\gamma}$ trimer association nor dissociation of $G_{\beta\gamma}$ from G_{α} (Reddy *et al.,* 2021). As conducted MD simulations also revealed that the I80T variant has no influence on SASA, radius of gyration and RMSD, and therefore no effect on folding, stability and dynamics of $G_{\beta\gamma}$, it is likely that the structural effect of I80T is further downstream in the cascade.

We show that the hydrogen bond pattern differs between the wt and I80T $G_{\beta\gamma}$. Compared to isoleucine that is hydrophobic in nature, threonine can form additional hydrogen bonds with surrounding residues. This is a new quality that could affect the behavior of the protein. We analyzed the hydrogen bonds of Thr80 to investigate the effect of the mutation on its surroundings. Even though interactions are present, low occurrence and variations in their occurrence among different MD runs indicate that stability of these

bonds on $G_{\beta\gamma}$ structure is minimal on our time scale of 500 ns. However, as conformational changes of proteins are naturally lengthier processes, the observed hydrogen bond pattern could have an effect on the structure or behavior of $G_{\beta\gamma}$ on longer time scales of MD simulations that can be investigated in future studies.

Analysis of G_{γ} RMSF suggests that while there is no visible effect of the I80T mutation on $G_{\beta\gamma}$ structure, the G_{γ} termini behave differently depending on whether $G_{\beta\gamma}$ is unbound or GIRK2-bound. This indicates an additional allosteric effect where dimer binding to GIRK2 influences G_{γ} behavior, despite G_{γ} not being a part of the GIRK2-$G_{\beta\gamma}$ binding interface. Therefore, a mutation not located directly in the binding interface could influence the interface allosterically. To an extent, this is supported by experimental data, where direct binding of $G_{\beta\gamma}$ to the CTD of GIRK2 was measured using *in vitro* pulldown assays. The binding of LoF variants I80N/T to the cytosolic domain of GIRK2 was reduced only by 25–30% compared to wt $G_{\beta\gamma}$. However, it is not yet known whether the GIRK2 CTD folds and tetramerizes properly in solution, and whether the absence of TMD influences GIRK2-$G_{\beta\gamma}$ affinity (Reddy *et al.,* 2021). As the binding of I80T $G_{\beta\gamma}$ to GIRK2 is reduced only in moderation, Reddy *et al.* suggest that the mutated $G_{\beta\gamma}$ induces additional allosteric conformational changes of GIRK2 that could cause deficiencies in channel gating. This proposes a plausible explanation that further needs to be tested in MD simulations containing the mutated $G_{\beta\gamma}$ and full GIRK2 tetrameric channel.

The C-terminus of G_{γ} ensures membrane attachment of the complex through the geranylgeranyl lipid tail. Studying GIRK2 activation in planar bilayer experiments in the presence of PIP_2 and prenylated or unprenylated $G_{\beta\gamma}$, prenylation of G_{γ} C-terminus has been shown to alter GIRK2 activation behavior (Wang *et al.,* 2014). While $G_{\beta\gamma}$ subunits deprived of the G_{γ} C-terminal geranylgeranyl tail did not cause robust opening of the channels, the addition of geranylgeranylated $G_{\beta\gamma}$ subunits to the same membrane resulted in large currents and robust GIRK2 channel opening. These results indicate that the geranylgeranyl lipid anchor is likely to be required for the maintenance of sufficient $G_{\beta\gamma}$ concentrations to activate GIRK2 channels (Wang *et al.,* 2014). However, the G_{γ} C-terminus in the 4KFM structure used in our MD simulations is unprenylated (Whorton & MacKinnon, 2013), and it is possible that the lipid anchor has additional influences. Therefore, further MD simulations containing prenylated G_{γ} C-terminus are required to assess the influence of geranylgeranyl lipid tail on the GIRK2-$G_{\beta\gamma}$ structure.

Overall, the results of our experiment indicate that the GNB1 encephalopathy causing mutation I80T does not influence the stability, conformation, folding,

compactness, and dynamics of $G_{\beta\gamma}$ in solution. We propose that the observed LoF effect of the I80T pathological variant results from allosteric changes that arise upon interaction of mutated $G_{\beta\gamma}$ with GIRK2. However, further MD simulation studies are required to establish the mechanisms of I80T allosteric regulation of GIRK2 channels. These are indicated to be performed on microsecond time scales, the structure shall contain the full complex of GIRK2-$G_{\beta\gamma}$, and the C-terminus of G_{γ} is recommended to be prenylated.

6 Conclusion

GIRK2 are inwardly rectifying ion channels responsible for the maintenance of the resting membrane potential. They are regulated by $G_{\beta\gamma}$, PIP_2 and Na^+ that act through a complex allosteric network to induce conformational changes of the channel and its gates to allow passage of K^+ ions. Mutations are known to be the leading cause of GIRK2 channelopathies. GNB1 encephalopathy is a heterogeneous neurodevelopmental syndrome caused by multiple mutations of the *GNB1* gene encoding for the G_β subunit, with the LoF I80T pathogenic variant being the most abundant among patients, causing excessive neuronal firing and seizures.

The focus of this study was to investigate how the I80T pathogenic variant impacts structure and dynamics of the $G_{\beta\gamma}$ subunit. Using MD simulations with the amber14sb force field, we were able to predict conformational and dynamical properties of the wt and mutant $G_{\beta\gamma}$. By analysis of MD simulation runs, we determined that the I80T variant does not impact the structure, conformation or dynamics of the $G_{\beta\gamma}$ dimer. We propose that the mutation exerts its pathological effect further downstream in the cascade by inducing allosteric changes upon interaction of $G_{\beta\gamma}$ with GIRK2 tetramers.

This study highlights that MD simulations are a valuable tool to be used for investigation of disease-associated mutations. However, the design of the experiment with the initial goal to limit computational power underlined the need to conduct further MD simulations of bigger systems that require greater computational power. In order to unravel the allosteric effect of I80T $G_{\beta\gamma}$ on GIRK2, we suggest to carry out MD simulations containing full complex of mutated $G_{\beta\gamma}$ bound to GIRK2 on microsecond time scales, and ensure that the G_γ C-terminus is prenylated. Elucidation of mutation-associated structural changes could help to understand pathological mechanisms and lead to an improvement of disease management and potential treatment options.

References

Abraham, M. J., Murtola, T., Schulz, R., Páll, S., Smith, J. C., Hess, B., & Lindahl, E. (2015). GROMACS: High performance molecular simulations through multi-level parallelism from laptops to supercomputers. *SoftwareX, 1-2,* 19–25. https://doi.org/10.1016/j.softx.2015.06.001

Adcock, S. A., & McCammon, J. A. (2006). Molecular dynamics: survey of methods for simulating the activity of proteins. *Chemical reviews*, *106*(5), 1589–1615. https://doi.org/10.1021/cr040426m

Baronas, V. A., & Kurata, H. T. (2014). Inward rectifiers and their regulation by endogenous polyamines. *Frontiers in physiology, 5*, 325. https://doi.org/10.3389/fphys.2014.00325

Bassani, D., & Moro, S. (2023). Past, Present, and Future Perspectives on Computer-Aided Drug Design Methodologies. *Molecules (Basel, Switzerland)*, *28*(9), 3906. https://doi.org/10.3390/molecules28093906

Berger, O., Edholm, O., & Jähnig, F. (1997). Molecular dynamics simulations of a fluid bilayer of dipalmitoylphosphatidylcholine at full hydration, constant pressure, and constant temperature. *Biophysical journal*, *72*(5), 2002–2013. https://doi.org/10.1016/S0006-3495(97)78845-3

Bernsteiner, H., Zangerl-Plessl, E. M., Chen, X., & Stary-Weinzinger, A. (2019). Conduction through a narrow inward-rectifier K^+ channel pore. *The Journal of general physiology*, *151*(10), 1231–1246. https://doi.org/10.1085/jgp.201912359

Bussi, G., Donadio, D., & Parrinello, M. (2007). Canonical sampling through velocity rescaling. *The Journal of chemical physics*, *126*(1), 014101. https://doi.org/10.1063/1.2408420

Cui, M., Cantwell, L., Zorn, A., & Logothetis, D. E. (2021). Kir Channel Molecular Physiology, Pharmacology, and Therapeutic Implications. *Handbook of experimental pharmacology*, *267*, 277–356. https://doi.org/10.1007/164_2021_501

Darden, T., York, D., & Pedersen, L. (1993). Particle mesh Ewald: An N·log(N) method for Ewald sums in large systems. *The Journal of Chemical Physics, 98*(12), 10089–10092. https://doi.org/10.1063/1.464397

Da Silva, J. D., Costa, M. D., Almeida, B., Lopes, F., Maciel, P., & Teixeira-Castro, A. (2021). Case Report: A Novel *GNB1* Mutation Causes Global Developmental Delay With Intellectual Disability and Behavioral Disorders. *Frontiers in neurology*, *12*, 735549. https://doi.org/10.3389/fneur.2021.735549

de Boer, T. P., Houtman, M. J., Compier, M., & van der Heyden, M. A. (2010). The mammalian K(IR)2.x inward rectifier ion channel family: expression pattern and pathophysiology. *Acta physiologica (Oxford, England)*, *199*(3), 243–256. https://doi.org/10.1111/j.1748-1716.2010.02108.x

De Vivo, M., Masetti, M., Bottegoni, G., & Cavalli, A. (2016). Role of Molecular Dynamics and Related Methods in Drug Discovery. *Journal of medicinal chemistry*, *59*(9), 4035–4061. https://doi.org/10.1021/acs.jmedchem.5b01684

Duc, N. M., Kim, H. R., & Chung, K. Y. (2015). Structural mechanism of G protein activation by G protein-coupled receptor. *European journal of pharmacology*, *763*(Pt B), 214–222. https://doi.org/10.1016/j.ejphar.2015.05.016

Durrant, J. D., & McCammon, J. A. (2011). Molecular dynamics simulations and drug discovery. *BMC biology*, *9*, 71. https://doi.org/10.1186/1741-7007-9-71

Evans, D. J., & Holian, B. L. (1985). The Nose–Hoover thermostat. *The Journal of Chemical Physics, 83*(8), 4069–4074. https://doi.org/10.1063/1.449071

Firth, H. V., Richards, S. M., Bevan, A. P., Clayton, S., Corpas, M., Rajan, D., Van Vooren, S., Moreau, Y., Pettett, R. M., & Carter, N. P. (2009). DECIPHER: Database of Chromosomal Imbalance and Phenotype in Humans Using Ensembl Resources. *American journal of human genetics*, *84*(4), 524–533. https://doi.org/10.1016/j.ajhg.2009.03.010

Fitzgerald, T. W., Gerety, S. S., Jones, W. D., van Kogelenberg, M., King, D. A., … Al-Turki, S. (2015). Deciphering Developmental Disorders Study. Large-scale discovery of novel genetic causes of developmental disorders. *Nature, 519*(7542), 223–228. https://doi.org/10.1038/nature14135

Friesacher, T., Reddy, H. P., Bernsteiner, H., Carlo Combista, J., Shalomov, B., Bera, A. K., Zangerl-Plessl, E. M., Dascal, N., & Stary-Weinzinger, A. (2022). A selectivity filter mutation provides

insights into gating regulation of a K+ channel. *Communications biology, 5*(1), 345. https://doi.org/10.1038/s42003-022-03303-1

Glaaser, I. W., & Slesinger, P. A. (2015). Structural Insights into GIRK Channel Function. *International review of neurobiology*, *123*, 117–160. https://doi.org/10.1016/bs.irn.2015.05.014

Guex, N., & Peitsch, M. C. (1997). SWISS-MODEL and the Swiss-PdbViewer: an environment for comparative protein modeling. *Electrophoresis*, *18*(15), 2714–2723. https://doi.org/10.1002/elps.1150181505

Hemati, P., Revah-Politi, A., Bassan, H., Petrovski, S., Bilancia, C. G., Ramsey, K., Griffin, N. G., Bier, L., Cho, M. T., Rosello, M., Lynch, S. A., Colombo, S., Weber, A., Haug, M., Heinzen, E. L., Sands, T. T., Narayanan, V., Primiano, M., Aggarwal, V. S., Millan, F., … Anyane-Yeboa, K. (2018). Refining the phenotype associated with GNB1 mutations: Clinical data on 18 newly identified patients and review of the literature. *American journal of medical genetics. Part A*, *176*(11), 2259–2275. https://doi.org/10.1002/ajmg.a.40472

Hess, B., Bekker, H., Berendsen, H. J. C., & Fraaije, J. G. E. M. (1997). LINCS: A linear constraint solver for molecular simulations. *Journal of Computational Chemistry, 18*(12), 1463–1472. https://doi.org/10.1002/(SICI)1096-987X(199709)18:12<1463::AID-JCC4>3.0.CO;2-H

Hibino, H., Inanobe, A., Furutani, K., Murakami, S., Findlay, I., & Kurachi, Y. (2010). Inwardly rectifying potassium channels: their structure, function, and physiological roles. *Physiological reviews*, *90*(1), 291–366. https://doi.org/10.1152/physrev.00021.2009

Higgins, J. B., & Casey, P. J. (1994). In vitro processing of recombinant G protein gamma subunits. Requirements for assembly of an active beta gamma complex. *The Journal of biological chemistry*, *269*(12), 9067–9073.

Hollingsworth, S. A., & Dror, R. O. (2018). Molecular Dynamics Simulation for All. *Neuron*, *99*(6), 1129–1143. https://doi.org/10.1016/j.neuron.2018.08.011

Hornak, V., Abel, R., Okur, A., Strockbine, B., Roitberg, A., & Simmerling, C. (2006). Comparison of multiple Amber force fields and development of improved protein backbone parameters. *Proteins*, *65*(3), 712–725. https://doi.org/10.1002/prot.21123

Huang, C. L., Feng, S., & Hilgemann, D. W. (1998). Direct activation of inward rectifier potassium channels by PIP2 and its stabilization by Gbetagamma. *Nature*, *391*(6669), 803–806. https://doi.org/10.1038/35882

Humphrey, W., Dalke, A., & Schulten, K. (1996). VMD: visual molecular dynamics. *Journal of molecular graphics*, *14*(1), 33–28. https://doi.org/10.1016/0263-7855(96)00018-5

Jeremic, D., Sanchez-Rodriguez, I., Jimenez-Diaz, L., & Navarro-Lopez, J. D. (2021). Therapeutic potential of targeting G protein-gated inwardly rectifying potassium (GIRK) channels in the central nervous system. *Pharmacology & therapeutics*, *223*, 107808. https://doi.org/10.1016/j.pharmthera.2021.107808

Jo, S., Kim, T., Iyer, V. G., & Im, W. (2008). CHARMM-GUI: a web-based graphical user interface for CHARMM. *Journal of computational chemistry*, *29*(11), 1859–1865. https://doi.org/10.1002/jcc.20945

Jones, H. F., Morales-Briceño, H., Barwick, K., Lewis, J., Sanchis-Juan, A., Raymond, F. L., Stewart, K., Waugh, M. C., Mahant, N., Kurian, M. A., Dale, R. C., & Mohammad, S. S. (2019). Myoclonus-dystonia caused by GNB1 mutation responsive to deep brain stimulation. *Movement disorders : official journal of the Movement Disorder Society*, *34*(7), 1079–1080. https://doi.org/10.1002/mds.27708

Jorgensen, W. L., Chandrasekhar, J., Madura, J. D., Impey, R. W., Klein, M. L. (1983). Comparison of simple potential functions for simulating liquid water. *The Journal of Chemical Physics, 79*(2), 926–935. https://doi.org/10.1063/1.445869

Kandt, C., Ash, W. L., & Tieleman, D. P. (2007). Setting up and running molecular dynamics simulations of membrane proteins. *Methods (San Diego, Calif.)*, *41*(4), 475–488. https://doi.org/10.1016/j.ymeth.2006.08.006

Karplus, M., & McCammon, J. A. (2002). Molecular dynamics simulations of biomolecules. *Nature structural biology*, *9*(9), 646–652. https://doi.org/10.1038/nsb0902-646

Khan, S. M., Sleno, R., Gora, S., Zylbergold, P., Laverdure, J. P., Labbé, J. C., Miller, G. J., & Hébert, T. E. (2013). The expanding roles of Gβγ subunits in G protein-coupled receptor signaling and drug action. *Pharmacological reviews*, *65*(2), 545–577. https://doi.org/10.1124/pr.111.005603

Kim J. B. (2014). Channelopathies. *Korean journal of pediatrics*, *57*(1), 1–18. https://doi.org/10.3345/kjp.2014.57.1.1

Kurata H. T. (2016). Emerging complexities of lipid regulation of potassium channels. *The Journal of general physiology*, *148*(3), 201–205. https://doi.org/10.1085/jgp.201611671

Lee, J., Hitzenberger, M., Rieger, M., Kern, N. R., Zacharias, M., & Im, W. (2020). CHARMM-GUI supports the Amber force fields. *The Journal of chemical physics*, *153*(3), 035103. https://doi.org/10.1063/5.0012280

Lee, S. J., Ren, F., Zangerl-Plessl, E. M., Heyman, S., Stary-Weinzinger, A., Yuan, P., & Nichols, C. G. (2016). Structural basis of control of inward rectifier Kir2 channel gating by bulk anionic phospholipids. *The Journal of general physiology*, *148*(3), 227–237. https://doi.org/10.1085/jgp.201611616

Li, D., Jin, T., Gazgalis, D., Cui, M., & Logothetis, D. E. (2019). On the mechanism of GIRK2 channel gating by phosphatidylinositol bisphosphate, sodium, and the Gβγ dimer. *The Journal of biological chemistry*, *294*(49), 18934–18948. https://doi.org/10.1074/jbc.RA119.010047

Liao, Y. J., Jan, Y. N., & Jan, L. Y. (1996). Heteromultimerization of G-protein-gated inwardly rectifying K+ channel proteins GIRK1 and GIRK2 and their altered expression in weaver brain. *The Journal of neuroscience : the official journal of the Society for Neuroscience*, *16*(22), 7137–7150. https://doi.org/10.1523/JNEUROSCI.16-22-07137.1996

Logothetis, D. E., Petrou, V. I., Zhang, M., Mahajan, R., Meng, X. Y., Adney, S. K., Cui, M., & Baki, L. (2015). Phosphoinositide control of membrane protein function: a frontier led by studies on ion channels. *Annual review of physiology*, *77*, 81–104. https://doi.org/10.1146/annurev-physiol-021113-170358

Lohmann, K., Masuho, I., Patil, D. N., Baumann, H., Hebert, E., Steinrücke, S., Trujillano, D., Skamangas, N. K., Dobricic, V., Hüning, I., Gillessen-Kaesbach, G., Westenberger, A., Savic-Pavicevic, D., Münchau, A., Oprea, G., Klein, C., Rolfs, A., & Martemyanov, K. A. (2017). Novel GNB1 mutations disrupt assembly and function of G protein heterotrimers and cause global developmental delay in humans. *Human molecular genetics*, *26*(6), 1078–1086. https://doi.org/10.1093/hmg/ddx018

Lopatin, A. N., Makhina, E. N., & Nichols, C. G. (1994). Potassium channel block by cytoplasmic polyamines as the mechanism of intrinsic rectification. *Nature*, *372*(6504), 366–369. https://doi.org/10.1038/372366a0

Lu Z. (2004). Mechanism of rectification in inward-rectifier K+ channels. *Annual review of physiology, 66,* 103–129. https://doi.org/10.1146/annurev.physiol.66.032102.150822

Lüscher, C., & Slesinger, P. A. (2010). Emerging roles for G protein-gated inwardly rectifying potassium (GIRK) channels in health and disease. *Nature reviews. Neuroscience*, *11*(5), 301–315. https://doi.org/10.1038/nrn2834

Mathiharan, Y. K., Glaaser, I. W., Zhao, Y., Robertson, M. J., Skiniotis, G., & Slesinger, P. A. (2021). Structural insights into GIRK2 channel modulation by cholesterol and PIP_2. *Cell reports*, *36*(8), 109619. https://doi.org/10.1016/j.celrep.2021.109619

Niu, Y., Tao, X., Touhara, K. K., & MacKinnon, R. (2020). Cryo-EM analysis of PIP_2 regulation in mammalian GIRK channels. *eLife*, *9*, e60552. https://doi.org/10.7554/eLife.60552

Parrinello, M., & Rahman, A. (1981). Polymorphic transitions in single crystals: A new molecular dynamics method. *Journal of Applied Physics, 52*(12), 7182–7190. https://doi.org/10.1063/1.328693

Pegan, S., Arrabit, C., Zhou, W., Kwiatkowski, W., Collins, A., Slesinger, P. A., & Choe, S. (2005). Cytoplasmic domain structures of Kir2.1 and Kir3.1 show sites for modulating gating and rectification. *Nature neuroscience*, *8*(3), 279–287. https://doi.org/10.1038/nn1411

Petrovski, S., Küry, S., Myers, C. T., Anyane-Yeboa, K., Cogné, B., Bialer, M., Xia, F., Hemati, P., Riviello, J., Mehaffey, M., Besnard, T., Becraft, E., Wadley, A., Politi, A. R., Colombo, S., Zhu, X., Ren, Z., Andrews, I., Dudding-Byth, T., Schneider, A. L., … Goldstein, D. B. (2016). Germline De Novo Mutations in GNB1 Cause Severe Neurodevelopmental Disability, Hypotonia, and Seizures. *American journal of human genetics*, *98*(5), 1001–1010. https://doi.org/10.1016/j.ajhg.2016.03.011

Reddy, H. P., Yakubovich, D., Keren-Raifman, T., Tabak, G., Tsemakhovich, V. A., Pedersen, M. H., Shalomov, B., Colombo, S., Goldstein, D. B., Javitch, J. A., Bera, A. K., & Dascal, N. (2021). Encephalopathy-causing mutations in Gβ1 (GNB1) alter regulation of neuronal GIRK channels. *iScience, 24*(9), 103018. https://doi.org/10.1016/j.isci.2021.103018

Revah-Politi, A., Sands, T.T., Colombo, S., Goldstein, D.B., and Anyane-Yeboa, K. (2020). GNB1 Encephalopathy. In: Adam, M.P., Feldman, J., Mirzaa, G.M., *et al.* (eds) Gene Reviews [Internet]. University of Washington, Seattle, 1993–2021. https://www.ncbi.nlm.nih.gov/books/NBK554743/

Rifkin, R. A., Moss, S. J., & Slesinger, P. A. (2017). G Protein-Gated Potassium Channels: A Link to Drug Addiction. *Trends in pharmacological sciences*, *38*(4), 378–392. https://doi.org/10.1016/j.tips.2017.01.007

Rubaiy H. N. (2017). A Short Guide to Electrophysiology and Ion Channels. *Journal of pharmacy & pharmaceutical sciences : a publication of the Canadian Society for Pharmaceutical Sciences, Societe canadienne des sciences pharmaceutiques*, *20*, 48–67. https://doi.org/10.18433/J32P6R

Schmidt, C. J., Thomas, T. C., Levine, M. A., & Neer, E. J. (1992). Specificity of G protein beta and gamma subunit interactions. *The Journal of biological chemistry*, *267*(20), 13807–13810.

Schrödinger, L. (2010). The PyMOL Molecular Graphics System, Version 2.0, LLC

Sondek, J., Bohm, A., Lambright, D. G., Hamm, H. E., & Sigler, P. B. (1996). Crystal structure of a G-protein beta gamma dimer at 2.1A resolution. *Nature*, *379*(6563), 369–374. https://doi.org/10.1038/379369a0

Tao, X., Avalos, J. L., Chen, J., & MacKinnon, R. (2009). Crystal structure of the eukaryotic strong inward-rectifier K+ channel Kir2.2 at 3.1 A resolution. *Science (New York, N.Y.)*, *326*(5960), 1668–1674. https://doi.org/10.1126/science.1180310

Turner, P. J. (2005). XMGRACE, Version 5.1.25, Center for Coastal and Land-Margin Research, Oregon Graduate Institute of Science and Technology

Wang, W., Touhara, K. K., Weir, K., Bean, B. P., & MacKinnon, R. (2016). Cooperative regulation by G proteins and Na(+) of neuronal GIRK2 K(+) channels. *eLife*, *5*, e15751. https://doi.org/10.7554/eLife.15751

Wang, W., Whorton, M. R., & MacKinnon, R. (2014). Quantitative analysis of mammalian GIRK2 channel regulation by G proteins, the signaling lipid PIP2 and Na+ in a reconstituted system. *eLife*, *3*, e03671. https://doi.org/10.7554/eLife.03671

Whorton, M. R., & MacKinnon, R. (2011). Crystal structure of the mammalian GIRK2 K+ channel and gating regulation by G proteins, PIP2, and sodium. *Cell*, *147*(1), 199–208. https://doi.org/10.1016/j.cell.2011.07.046

Whorton, M. R., & MacKinnon, R. (2013). X-ray structure of the mammalian GIRK2-βγ G-protein complex. *Nature*, *498*(7453), 190–197. https://doi.org/10.1038/nature12241

Wolber, G., & Langer, T. (2005). LigandScout: 3-D pharmacophores derived from protein-bound ligands and their use as virtual screening filters. *Journal of chemical information and modeling*, *45*(1), 160–169. https://doi.org/10.1021/ci049885e

Zhang, F. L., & Casey, P. J. (1996). Protein prenylation: molecular mechanisms and functional consequences. *Annual review of biochemistry*, *65*, 241–269. https://doi.org/10.1146/annurev.bi.65.070196.001325

Zoete, V., Cuendet, M. A., Grosdidier, A., & Michielin, O. (2011). SwissParam: a fast force field generation tool for small organic molecules. *Journal of computational chemistry*, *32*(11), 2359–2368. https://doi.org/10.1002/jcc.21816

Internet references

www1: GNB1 Foundation [accessed. 2023-10-23]
<https://www.gnb1.org>
www2: Manual Gromacs [accessed. 2023-04-24]
<https://doi.org/10.5281/zenodo.8134388>

Supplementary

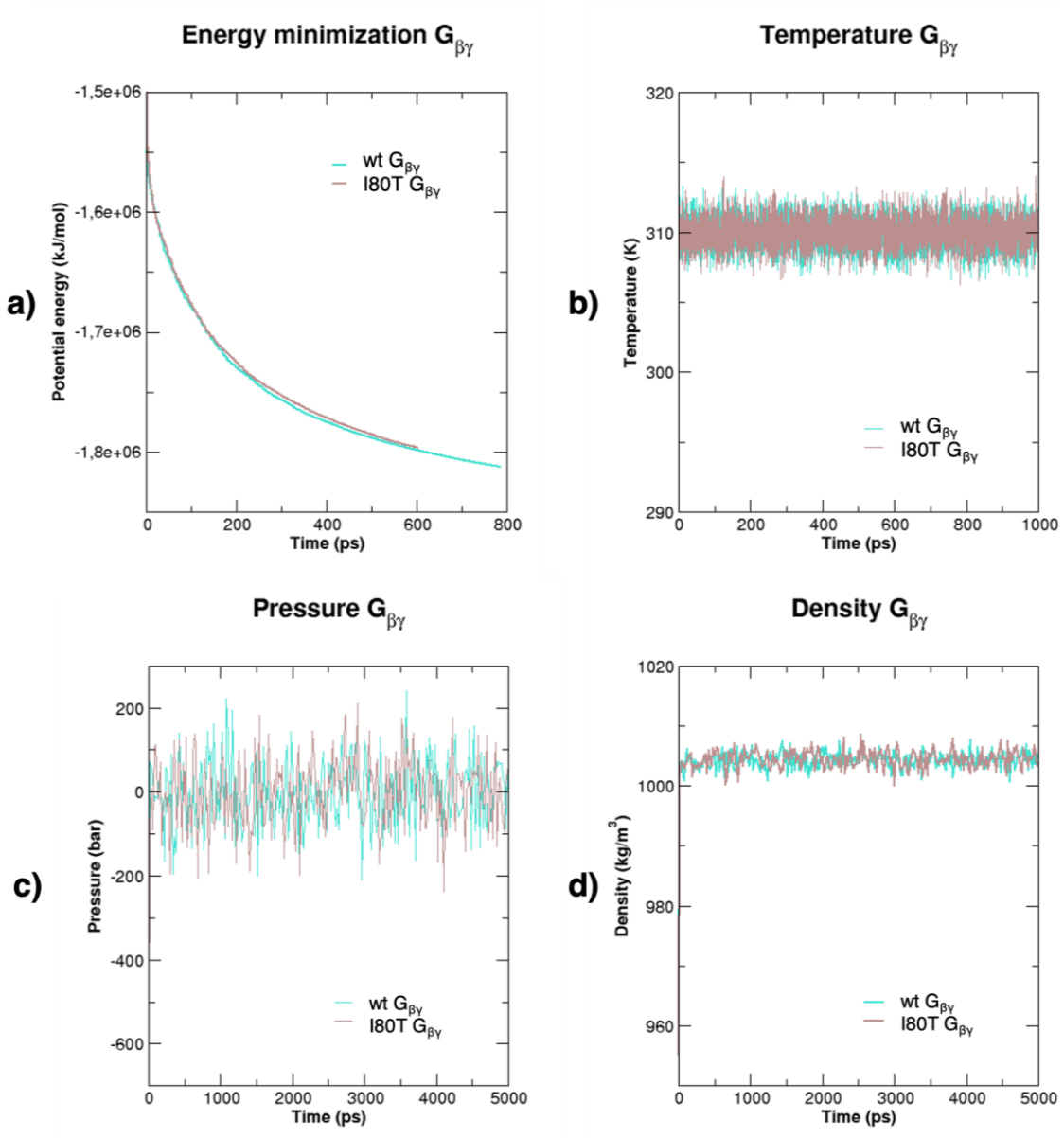

Figure S1 – Thermodynamic properties of system equilibration prior to MD simulation free runs. Data for wt $G_{\beta\gamma}$ is shown in turquoise and data for I80T $G_{\beta\gamma}$ is shown in pink. **a) Energy minimization.** Appropriate geometry without steric clashes and local minimum of energy was ensured, demonstrated by a steady convergence of potential energy in the plot. **b) Temperature.** Physiological temperature of the system was reached and stabilized by the NVT equilibration step. As seen from the plot, temperature reached its stable target plateau value at 310 K, small fluctuations are allowed. **c) Pressure.** Pressure was stabilized during the NPT equilibration step. It is natural for pressure to fluctuate to this extent during simulations of aqueous solutions. **d) Density.** As with the pressure, density was stabilized with NPT equilibration. Average values of density were stable and close to the experimental value of 1000 kg/m^3, indicating proper equilibration of the system ready for MD simulations.

Table S1 – Summary of selected descriptive parameters to assess structural and trajectory changes of wt $G_{\beta\gamma}$, I80T $G_{\beta\gamma}$ and ETX $G_{\beta\gamma}$. Following parameters are shown: number of hydrogen bonds formed between G_{β} and G_{γ}, SASA, radius of gyration, and RMSD values for backbone and protein of $G_{\beta\gamma}$. The table displays data from all timeframes of 3 MD runs unbound $G_{\beta\gamma}$ (shown in pink) and 4 GIRK2-bound $G_{\beta\gamma}$ subunits (shown in grey). Average values are also show in separate tables in the Results section.

	Hydrogen bonds (#)	SASA (nm2)	Radius of gyration (nm)	RMSD backbone (nm)	RMSD protein (nm)
	wt Gβγ				
MD run 1	20.0074	178.2492	2.1675	0.1994	0.2599
MD run 2	19.8920	178.8185	2.1738	0.1977	0.2636
MD run 3	19.4400	178.2340	2.1746	0.2270	0.2912
average	**19.78**	**178.43**	**2.172**	**0.208**	**0.272**
	I80T Gβγ				
MD run 1	19.5114	178.8825	2.1725	0.2230	0.2915
MD run 2	18.0336	177.6780	2.1668	0.2293	0.2952
MD run 3	21.8498	174.7508	2.1645	0.2342	0.3022
average	**19.80**	**177.10**	**2.168**	**0.229**	**0.296**
	ETR+10mV				
Gβγ 1	21.704	179.4320	2.1665	0.1891	0.2446
Gβγ 2	19.859	179.7215	2.1667	0.1794	0.2397
Gβγ 3	17.513	181.6232	2.1764	0.2104	0.2748
Gβγ 4	16.284	185.6002	2.1862	0.2418	0.2952
average	**18.84**	**181.59**	**2.174**	**0.205**	**0.264**
	ETR-10mV				
Gβγ 1	22.223	182.2475	2.1760	0.2367	0.2764
Gβγ 2	15.635	183.8049	2.1848	0.1939	0.2558
Gβγ 3	16.932	183.1105	2.1855	0.1352	0.2026
Gβγ 4	17.954	182.8046	2.1818	0.1718	0.2435
average	**18.19**	**182.99**	**2.182**	**0.184**	**0.245**
	ETS+10mV				
Gβγ 1	19.601	180.1230	2.1665	0.2003	0.2539
Gβγ 2	20.151	179.8055	2.1657	0.1593	0.2181
Gβγ 3	18.583	183.2989	2.1726	0.1996	0.2704
Gβγ 4	19.253	181.8043	2.1592	0.1856	0.2495
average	**19.40**	**181.26**	**2.166**	**0.186**	**0.248**
	ETS-10mV				
Gβγ 1	25.028	179.6762	2.1609	0.1703	0.2359
Gβγ 2	19.718	186.5556	2.1963	0.2214	0.2710
Gβγ 3	16.489	183.9294	2.1803	0.1755	0.2388
Gβγ 4	15.318	186.2784	2.1778	0.1849	0.2540
average	**19.14**	**184.11**	**2.179**	**0.188**	**0.250**

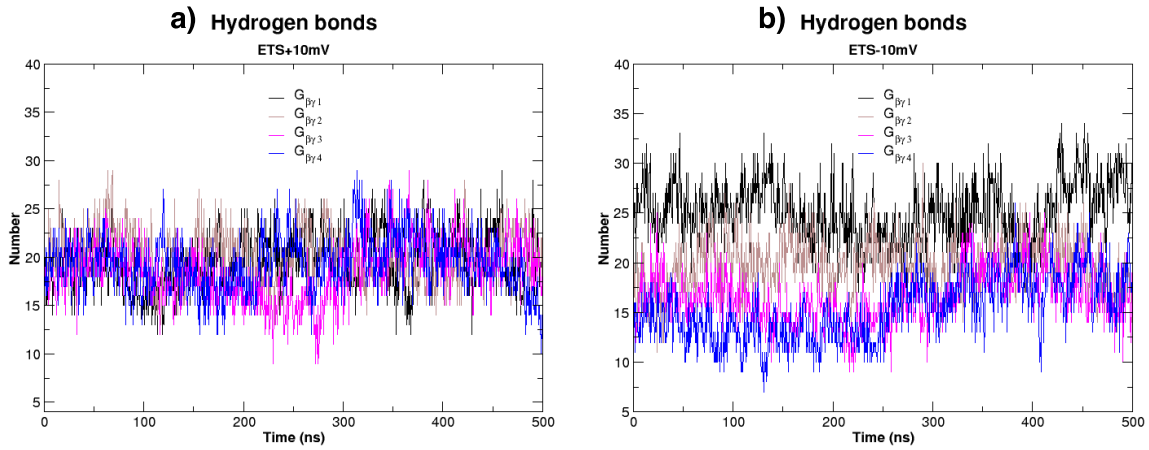

Figure S2 – Number of hydrogen bonds formed between G_β and G_γ throughout simulations (ETS). Hydrogen bonds for pairs within 0.35 nm are displayed for 4 $G_{\beta\gamma}$ subunits per 1 500 ns long MD run. Bonds between G_β and G_γ of GIRK2-bound $G_{\beta\gamma}$ are shown in **a)** ETS +10 mV and **b)** ETS -10 mV.

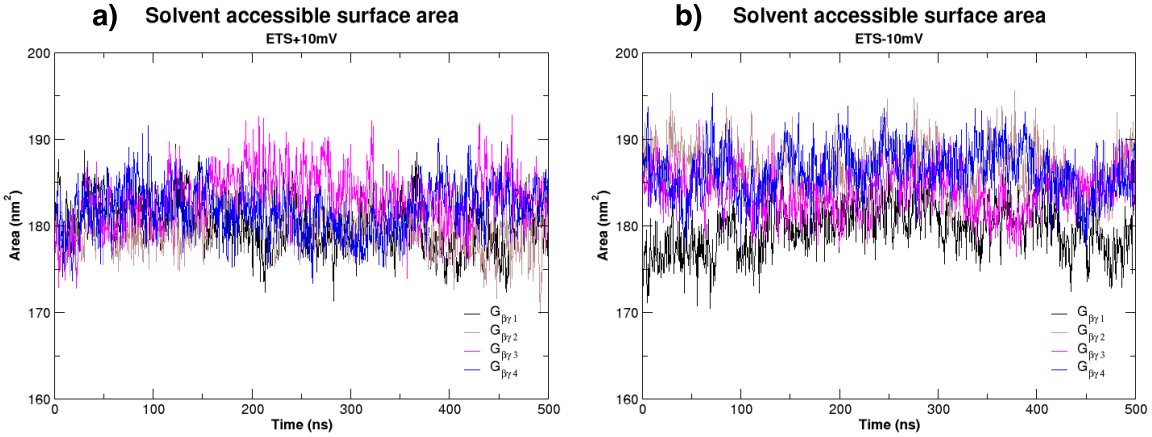

Figure S3 – Solvent accessible surface area of $G_{\beta\gamma}$ throughout simulations (ETS). SASA in nm^2 is displayed for 4 $G_{\beta\gamma}$ subunits per 1 500 ns long MD run. Data for GIRK2-bound $G_{\beta\gamma}$ is shown for **a)** ETS +10 mV and **b)** ETS -10 mV.

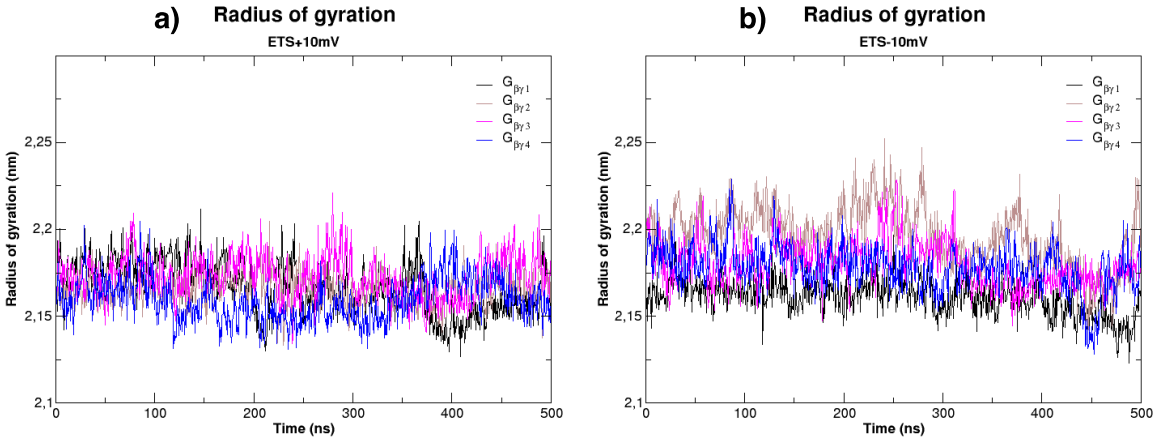

Figure S4 – Radius of gyration for $G_{\beta\gamma}$ throughout simulations (ETS). Radius of gyration in nm is shown for 4 $G_{\beta\gamma}$ subunits per 1 500 ns long MD run of GIRK2-bound $G_{\beta\gamma}$ in **a)** ETS +10 mV and **b)** ETS -10 mV.

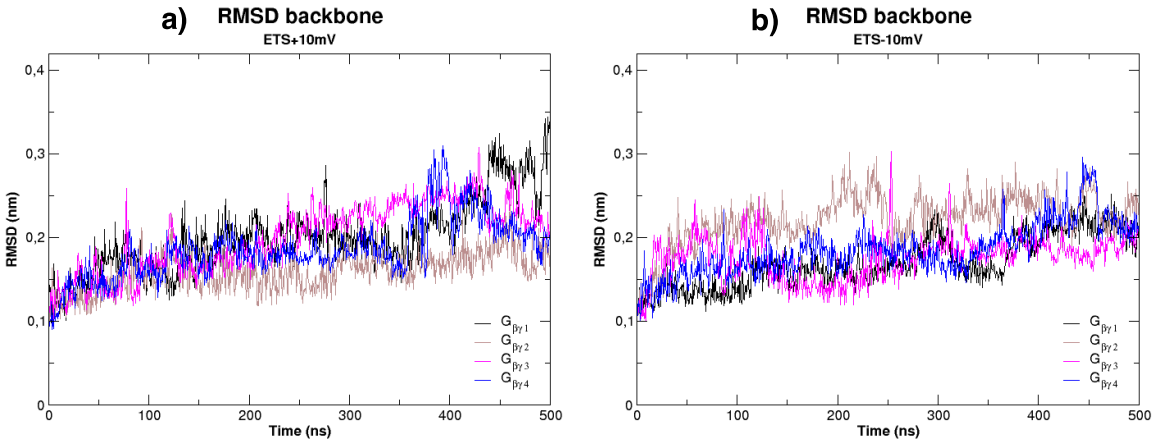

Figure S5 – RMSD of $G_{\beta\gamma}$ backbone after 1sq fit to backbone throughout simulations (ETS). RMSD in nm is shown relative to the structure of the minimized, equilibrated system. RMSD is shown for 4 $G_{\beta\gamma}$ subunits per 1 500 ns long MD run of GIRK2-bound $G_{\beta\gamma}$ in **a)** ETS +10 mV and **b)** ETS -10 mV.

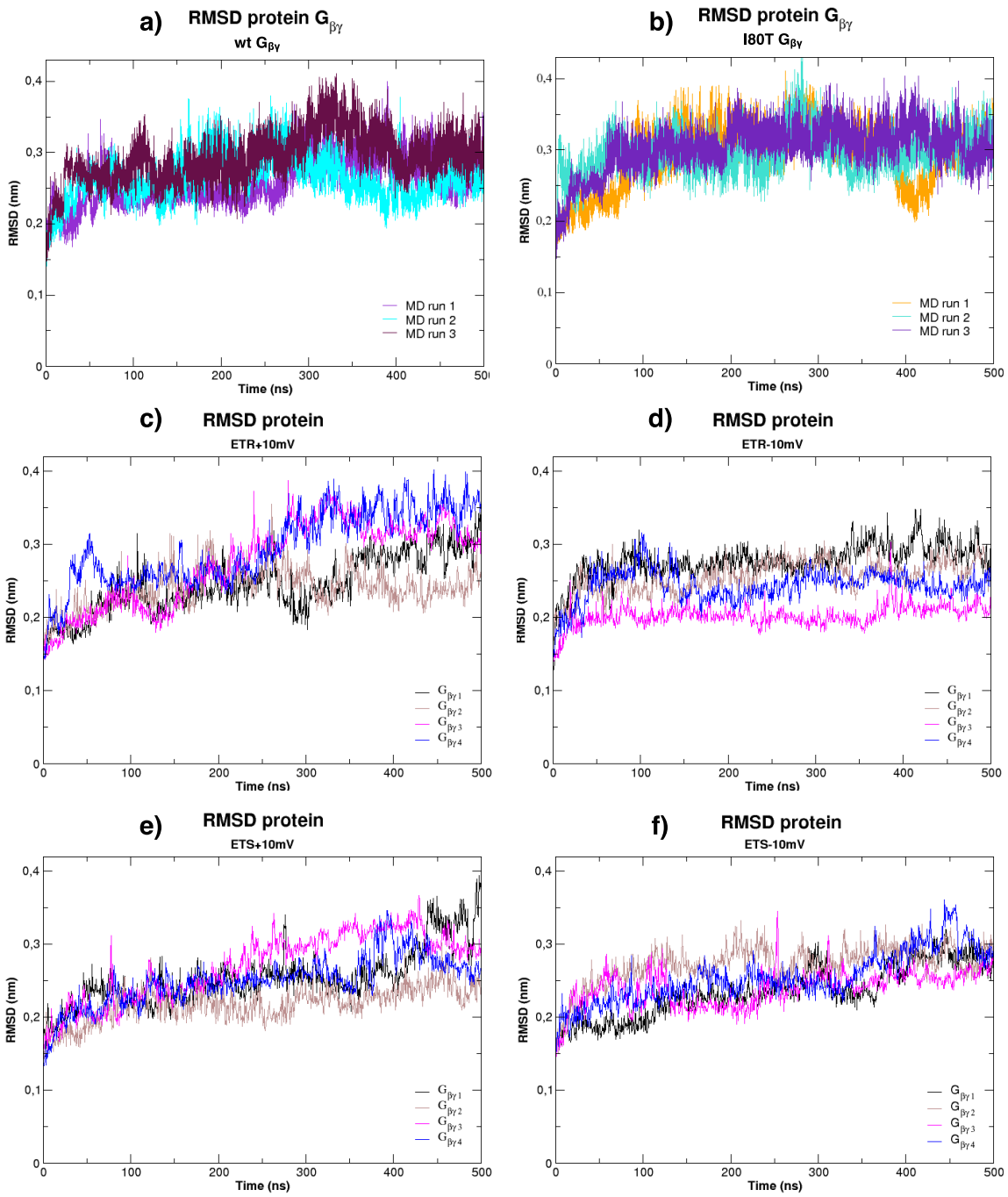

Figure S6 – RMSD of $G_{\beta\gamma}$ protein after 1sq fit to protein throughout simulations. RMSD in nm is shown relative to the structure of the minimized, equilibrated system. RMSD of unbound $G_{\beta\gamma}$ is shown for **a)** wt $G_{\beta\gamma}$ and **b)** I80T $G_{\beta\gamma}$. Data for GIRK2-bound $G_{\beta\gamma}$ is represented in **c)** and **d)** where data from ETR simulations is shown, and in **e)** and **f)** where ETS data is displayed.

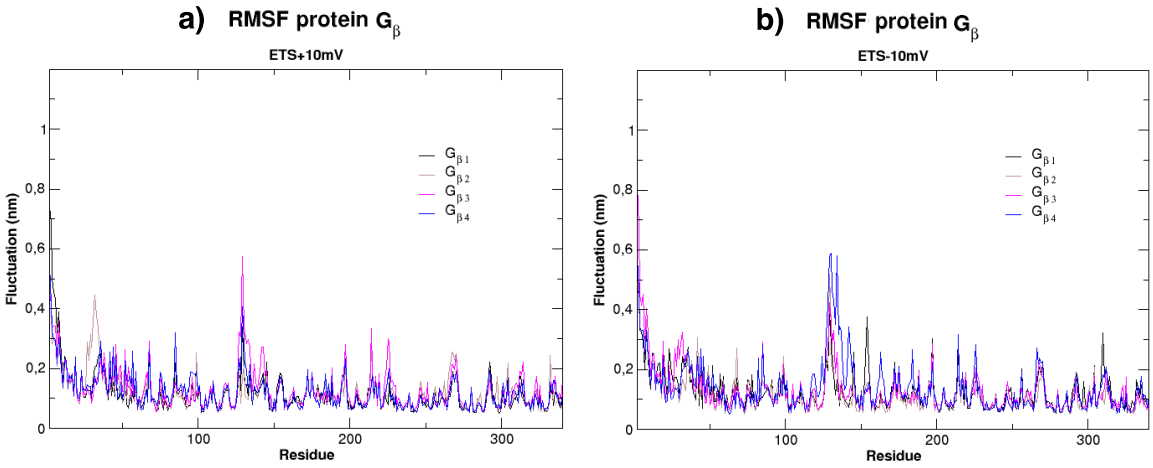

Figure S7 – RMSF of G_{β} protein throughout simulations (ETS). RMSF in nm is shown relative to the structure of the minimized, equilibrated system as the square root of variance of fluctuation around the average position. RMSF is shown for 4 $G_{\beta\gamma}$ subunits per 1 500 ns long MD run of GIRK2-bound $G_{\beta\gamma}$ in **a)** ETS +10 mV and **b)** ETS -10 mV.

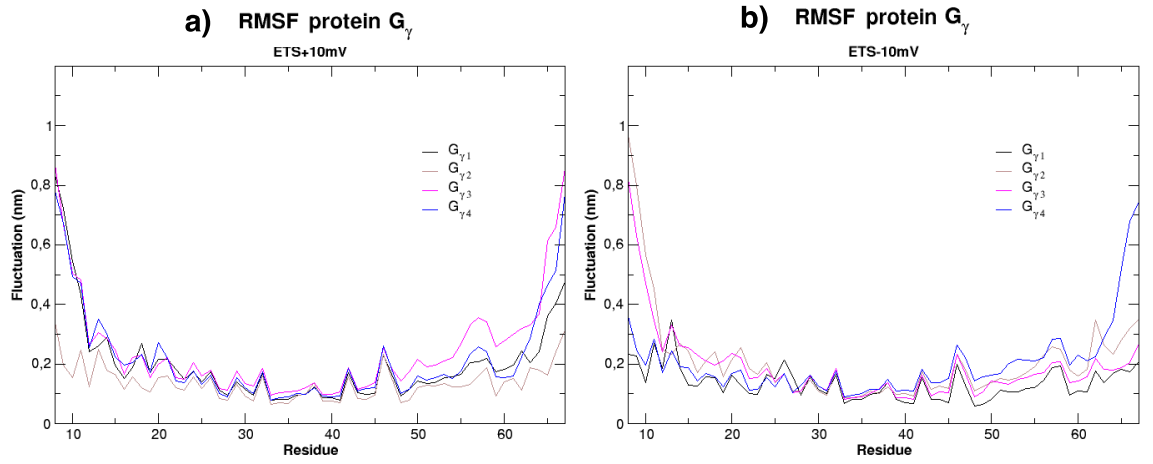

Figure S8 – RMSF of G_{γ} protein throughout simulations (ETS). RMSF in nm is shown relative to the structure of the minimized, equilibrated system as the square root of variance of fluctuation around the average position. RMSF is shown for 4 $G_{\beta\gamma}$ subunits per 1 500 ns long MD run of GIRK2-bound $G_{\beta\gamma}$ in **a)** ETS +10 mV and **b)** ETS -10 mV.

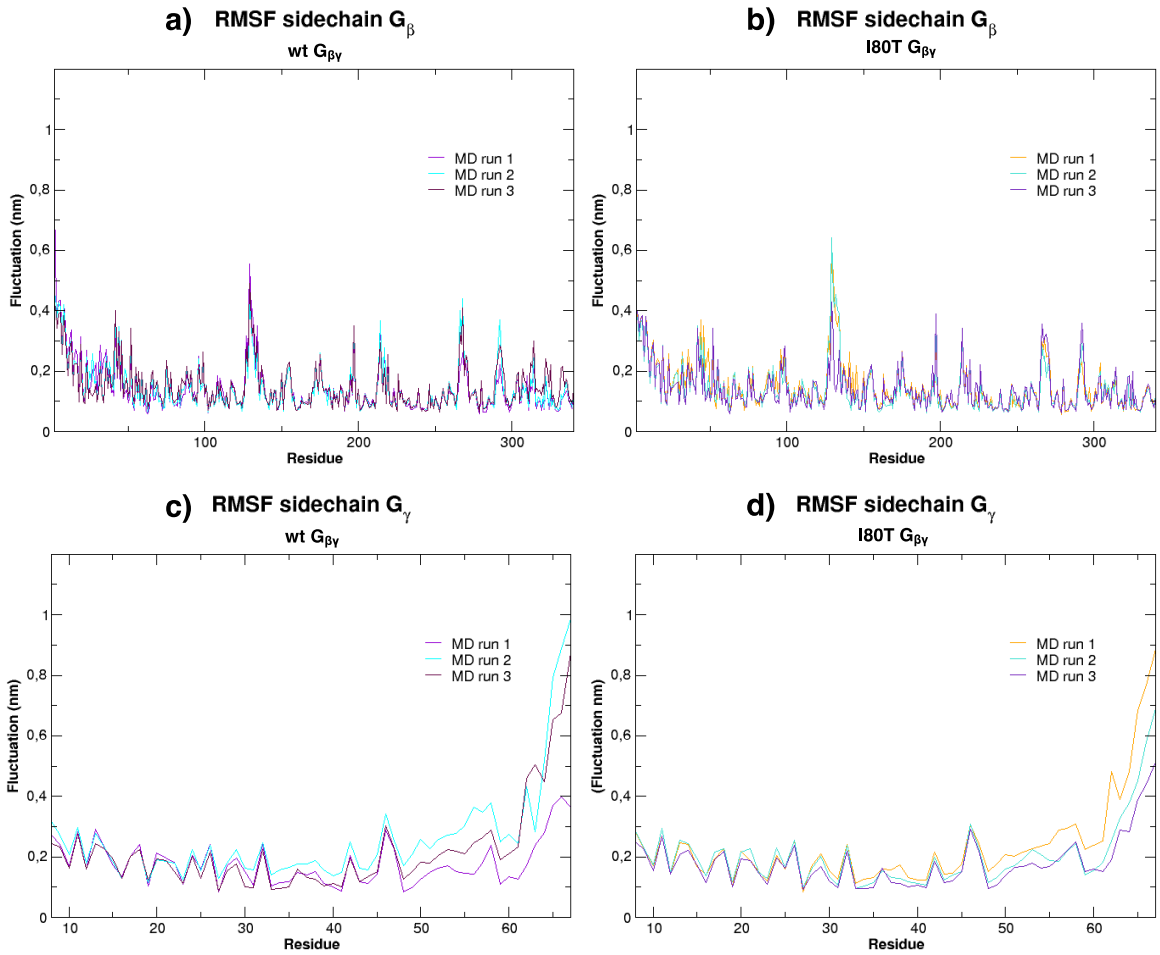

Figure S9 – RMSF of G_β and G_γ side chain for wt and I80T structures throughout simulations. RMSF in nm is shown relative to the structure of the minimized, equilibrated system as the square root of variance of fluctuation around the average position. Side chain RMSF values of unbound G_β are shown for **a)** wt $G_{\beta\gamma}$ and **b)** I80T $G_{\beta\gamma}$ and of unbound G_γ for **c)** wt $G_{\beta\gamma}$ and **d)** I80T $G_{\beta\gamma}$.